

ASTEROID SPECTROSCOPY: I. A THERMAL  
INFRARED SURVEY OF ASTEROIDS II. X-RAY  
FLUORESCENCE SPECTROSCOPY OF 433  
EROS

A Dissertation

Presented to the Faculty of the Graduate School

of Cornell University

in Partial Fulfillment of the Requirements for the Degree of

Doctor of Philosophy

by

Lucy F. Lim

January 2005

© 2004 Lucy F. Lim

ALL RIGHTS RESERVED

## TABLE OF CONTENTS

<b>1</b>	<b>Introduction</b>	<b>1</b>
<b>2</b>	<b>Thermal Infrared (8-13 <math>\mu\text{m}</math>) Spectra of 29 Asteroids: The Cornell Mid-Infrared Asteroid Spectroscopy (“MIDAS”) Survey</b>	<b>3</b>
2.1	Introduction . . . . .	3
2.2	Observations . . . . .	5
2.3	Calibration and Processing . . . . .	13
2.4	Sources of Uncertainty . . . . .	18
2.5	Radius and temperature fits: the standard thermal model	29
2.5.1	Limitations of the standard thermal model . . . . .	31
2.5.2	Fits to the STM . . . . .	33
2.6	Results . . . . .	37
2.7	Discussions of Individual Asteroids . . . . .	44
2.7.1	1 Ceres . . . . .	44
2.7.2	2 Pallas . . . . .	46
2.7.3	3 Juno . . . . .	47
2.7.4	4 Vesta . . . . .	48
2.7.5	10 Hygiea . . . . .	52
2.7.6	433 Eros . . . . .	56
2.7.7	M-class Asteroids . . . . .	57
2.7.8	Other Asteroids that Depart from the STM . . . . .	61
2.8	Interpretation . . . . .	63
2.8.1	Thermal Properties . . . . .	64

2.9	Conclusions . . . . .	70
<b>3</b>	<b>X-ray Fluorescence Spectroscopy of 433 Eros: Background</b>	<b>85</b>
3.1	Overview . . . . .	85
3.2	The Solar X-ray Spectrum . . . . .	88
3.2.1	Theoretical Models of the Solar X-ray Spectrum . . .	91
3.3	The NEAR gas proportional counter . . . . .	95
3.3.1	Energy Resolution . . . . .	96
3.3.2	Escape Peak . . . . .	97
3.3.3	Limitations of the gas solar monitor . . . . .	98
3.4	The Graded Filter . . . . .	100
3.5	Modelling the Solar Monitor Response . . . . .	104
3.5.1	Attenuation of the Graded Filter . . . . .	104
3.5.2	Other Aspects of the Detector Response . . . . .	110
3.5.3	The Chi-Squared Fitting Process . . . . .	111
3.5.4	Checking the Model Results . . . . .	112
3.6	The NEAR Asteroid-Pointing Detectors . . . . .	114
3.7	Interaction of Solar X-rays with a Planetary Surface . . . .	116
3.7.1	Primary X-ray Production in a Surface . . . . .	116
3.7.2	X-Ray Background: Coherent and Incoherent Scatter	119
<b>4</b>	<b>Results of the XRS Investigation</b>	<b>122</b>
4.1	Solar Fitting Results . . . . .	122
4.1.1	Theoretical Models . . . . .	122
4.1.2	Graded filter characteristics . . . . .	132

4.1.3	Model Selection and Comparison . . . . .	142
4.1.4	An Example of Solar Flare Fitting . . . . .	143
4.2	Interpreting the Asteroid-Pointing Data . . . . .	147
4.2.1	Calibration with the Calibration Sources . . . . .	147
4.2.2	Extracting the photon counts . . . . .	150
4.3	Photon Ratio to Element Ratio Conversion . . . . .	157
4.4	Specific Solar Flares . . . . .	163
4.4.1	4 May 2000 . . . . .	163
4.4.2	20 May 2000 . . . . .	164
4.4.3	15 June 2000 . . . . .	166
4.4.4	17 June 2000 . . . . .	169
4.4.5	10 July 2000 . . . . .	169
4.4.6	27 December 2000 . . . . .	173
4.4.7	28 December 2000 . . . . .	176
4.4.8	2 January 2001 . . . . .	177
4.5	Results and Discussion . . . . .	179
4.6	Future Work . . . . .	193
4.6.1	Future XRF Experiments . . . . .	194

## LIST OF TABLES

2.1	Circumstances of Asteroid Observations . . . . .	7
2.2	STM temperature and radius fitting results. “Published radius” values are from the Supplemental IRAS Minor Planet Survey (Tedesco <i>et al.</i> , 2002) except where noted. The “assumed albedo” is the albedo used to calculate the “STM Predicted $T_{\text{subsolar}}$ .” These albedos have been taken from Tedesco <i>et al.</i> (2002) except as follows: 3 Juno and 4 Vesta, Morrison (1974); 9 Metis and 24 Themis, Giorgini <i>et al.</i> (1996); 433 Eros, Morrison (1976). “Rotation Period”: Giorgini <i>et al.</i> (1996); Harris (1996). . . . .	34
3.1	XRF-related Physical Constants . . . . .	87
3.2	Solar Coronal Abundances Relative to Si (Si = 100) . . . . .	94
3.3	Sample attenuation coefficients for proportional counter materials (cm) (Hubbell and Seltzer, 1997) . . . . .	104
3.4	Dimensions and engineering tolerances for the graded filter	105
3.5	Kapton composition from NIST . . . . .	106
3.6	Delrin composition from NIST . . . . .	106
3.7	Sample Scattering vs. Photoelectric Absorption Cross Sections . . . . .	121
4.1	Solar Element Ratios for Selected Elements: Meyer (1985) vs. Feldman (1992) . . . . .	128
4.2	Solar Monitor Data used in $\chi^2$ and GOES fitting . . . . .	133
4.3	Median $\chi^2$ for Best Two-Temperature Fits to 160 NEAR Spectra Using Various Graded Filter Models (Composite CHIANTI+MEKAL Models) . . . . .	134
4.4	Median $\chi^2$ for Best Two-Temperature Fits to 160 NEAR Spectra Using Various Graded Filter Models (Composite CHIANTI+MEKAL Models) . . . . .	135

4.5	Median $\chi^2$ for Best Two-Temperature Fits to 160 NEAR Spectra Using Various Graded Filter Models (Composite CHIANTI+MEKAL Models) . . . . .	136
4.6	Median $\chi^2$ for Best Two-Temperature Fits to 160 NEAR Spectra Using Various Graded Filter Models (New CHIANTI Models) . . . . .	137
4.7	Median $\chi^2$ for Best Two-Temperature Fits to 160 NEAR Spectra Using Various Graded Filter Models (New CHIANTI Models) . . . . .	138
4.8	Median $\chi^2$ for Best Two-Temperature Fits to 160 NEAR Spectra Using Various Graded Filter Models (New CHIANTI Models) . . . . .	139
4.9	Selected Graded Filter Models. All percentages refer to changes from the specified dimensions in Table 3.4. . . . .	144
4.10	Solar Fitting Results for a Flare (2000-June-17): Composite Model . . . . .	145
4.11	Solar Fitting Results for a Flare (2000-June-17): New CHIANTI Coronal . . . . .	146
4.12	XRS Asteroid-Pointing Detector Calibration Data Fitting Results . . . . .	151
4.13	Unfiltered Detector Characteristics Derived from Flare Data	151
4.14	Geometric Information for Eight Solar Flares . . . . .	157
4.15	Photon Counts and Ratios for Eight Solar Flares . . . . .	158
4.16	Meteorite Samples Used to Convert Photon Ratios to Element Ratios . . . . .	160
4.17	Effect of mineral mixing vs. homogeneous compositions for predicted x-ray fluorescence ratios. After Nittler et al. (2001) . . . . .	163
4.18	Photon and Element Ratios from Nittler et al. (2001) . . . . .	184
4.19	Element Ratios for Eight Solar Flares, Corrected for Mixing Effects: Model 1 . . . . .	185

4.20	Element Ratios for Eight Solar Flares, Corrected for Mixing Effects: Model 2 . . . . .	186
4.21	Element Ratios for Eight Solar Flares, Corrected for Mixing Effects: Model 3 . . . . .	187
4.22	Element Ratios for Eight Solar Flares, Corrected for Mixing Effects: Model 4 . . . . .	188
4.23	Element Ratios for Eight Solar Flares, Corrected for Mixing Effects: Model 5 . . . . .	189
4.24	Element Ratios for Eight Solar Flares, Corrected for Mixing Effects: Model 6 . . . . .	190
4.25	Element Ratios for Eight Solar Flares, Corrected for Mixing Effects: Model 7 . . . . .	191
4.26	Average Elemental Ratios Derived from Eight Solar Flares (Including Mineral-Mixing Corrections) . . . . .	192



## LIST OF FIGURES

2.1	Ratio of the spectrum of $\alpha$ Tauri published by Cohen <i>et al.</i> (1992) to the blackbody spectrum used as a reference for this star by Gillett and Merrill (1975). . . . .	5
2.2	SC-10 Dewar and Optics . . . . .	9
2.3	a. Background subtraction via on-chip chopping and nodding. b. Spatial profile. This is the sum across all wavelengths of the SC-10 detector signal from one segment. The central peak represents the two overlapping positive images. The flanking images represent the opposite chop positions. c. Raw data from the same SC-10 segment as a two-dimensional image. The spectral dispersion is left-right, with wavelength increasing toward the left. The vertical direction is spatial. . . . .	21
2.4	Spectra of $\gamma$ Aquilae ratioed to a 4000 K blackbody. Top: $\gamma$ Aql as measured in the current work. This spectrum is an average of three spectra calibrated on $\alpha$ Lyrae and $\beta$ Pegasi. Bottom: Template spectrum published for $\gamma$ Aql by Cohen <i>et al.</i> (1999). The template is based on $\alpha$ Hydrae shortward of $10.3\ \mu\text{m}$ and on a theoretical model longward of $10.6\ \mu\text{m}$ . . . . .	23
2.5	Model atmospheric transmission for Palomar (ATRAN, Lord (1992)). Atmospheric transmission as a function of wavelength in the mid-infrared. The large absorption between $9.2$ and $10.1\ \mu\text{m}$ is caused by telluric ozone; most of the other structure is due to water vapor. The transmission function has been smoothed to the spectral resolution of SC-10's low-resolution mode. . . . .	24

2.6	Wavelength registration of SC-10 data. Upper plot: Non-flux-calibrated spectral data from an asteroid (dot-dashed line) and a standard star (solid line). The shaded areas mark strong telluric features. Lower plot: Ratios of asteroid to standard spectra. The solid line here is the ratio of the correctly wavelength-calibrated raw spectra; the dotted line is the ratio when the source and standard spectra are misregistered in wavelength with respect to each other. Incorrect wavelength registration of the raw spectra causes substantial artifacts in the ratio at wavelengths where there is a slope in the atmospheric transmission function. . . . .	25
2.7	Mid-infrared spectra of laboratory materials. a. Effects of particle size on the strength of mid-infrared spectral features. At small grain sizes the features are suppressed but do not change in wavelength. Data from Salisbury <i>et al.</i> (1991). b. Powdered meteorite samples at fine (0–74 $\mu\text{m}$ ) particle sizes. Data from Salisbury <i>et al.</i> (1991). The Allende and Johnstown spectra have been offset by 1.5% and 3% respectively from La Criolla for clarity. The right-hand axis is emissivity derived from bidirectional reflectance data (Footnote 9) for easier comparison with the current work. . . . .	27
2.8	Mid-infrared flux spectra of the twenty-nine “MIDAS” asteroids. The data have been binned to 0.1 $\mu\text{m}$ resolution. The error bars represent the standard deviation of the points in each bin. The dashed lines represent the best-fit STM for each spectrum. The shaded grey areas are regions of strong telluric absorptions. Data points within those wavelength regions should be regarded as suspect. .	38
2.9	Emissivity spectra of selected asteroids. These were produced by dividing the flux spectra in Figure 2.8 by the best-fit STM thermal models. Again, the grey shaded areas represent wavelength regions where the data are prone to systematic errors due to strong telluric absorption features.	43
2.10	Thermal Infrared Spectra of 4 Vesta and various laboratory materials. Laboratory data from Salisbury <i>et al.</i> (1991) and Salisbury <i>et al.</i> (1991) For the relationship between biconical reflectance and emissivity, see footnote in “Interpretation”. . . . .	49

2.11	MIDAS and ISO sub-Earth points and fields of view for 4 Vesta. Shaded areas are within $70^\circ$ of the sub-Earth point. The pole solution used was $[301^\circ, 41^\circ]$ (Thomas <i>et al.</i> , 1997). See Table 1.3 for the times and coordinates of each measurement. . . . .	51
2.12	MIDAS and ISO sub-Earth points and fields of view for 10 Hygiea. Again, points within $70^\circ$ of the sub-Earth point are considered to be inside the field of view. See Table 1.4 for the times and coordinates of each measurement. The ISO SWS observation lasted for over three hours, so we have represented both its starting and ending sub-Earth points on the map joined by a line. Top: Sub-Earth points calculated using the “p3” pole solution, $[120^\circ, 34^\circ]$ . Bottom: Sub-Earth points calculated using the “p4” pole solution, $[295^\circ, 43^\circ]$ . . . . .	54
2.13	Rotation rates and MIDAS radii. Asteroid measurements with unusually high ( $\eta > 0.85$ ) beaming parameters are marked with diamonds. . . . .	67
2.14	Derived beaming parameters ( $\eta$ ) vs. phase angles of MIDAS observation. . . . .	69
3.1	X-ray fluorescence illustrated. . . . .	86
3.2	Theoretical single-temperature solar spectra at three temperatures. (Mewe et al., 1985) . . . . .	89
3.3	Single-temperature (top) vs. two-temperature fit to a NEAR solar monitor spectrum. The smooth traces are the models, while the jagged ones are the NEAR data. In the lower plot, the dotted lines are the two isothermal components of the fit. . . . .	92
3.4	Schematic diagram of a gas proportional counter. From Knoll (2000) . . . . .	98
3.5	Schematic cross-section of the graded filter pinhole with nominal dimensions . . . . .	101
3.6	Engineering diagram of the graded filter . . . . .	102
3.7	Ray paths through the graded filter. . . . .	109

3.8	GOES-8 transfer functions. . . . .	113
3.9	Detector efficiency vs. energy for the asteroid-pointing proportional counters, including the effects of the balanced filters. From Starr et al. (2000). . . . .	115
4.1	Two-Temperature Fits Using CHIANTI-Photospheric Spectra. The dotted lines represent the individual isothermal components of the fit. The solid line is the sum of the two isothermal components, zero-shifted to match the data. The fainter, noisy solid line is the actual spectrum from the gas solar monitor. . . . .	124
4.2	Two-Temperature Fits Using CHIANTI-Coronal Spectra. The noisy line is the 50-second solar monitor spectrum; the smooth solid line is the 2003 CHIANTI model. See Fig. 4.1. . . . .	125
4.3	Two-Temperature Fits Using Composite Mewe and CHIANTI-Coronal Model Spectra. The noisy line is the 50-second solar monitor spectrum; the smooth solid line is the composite CHIANTI-Coronal + Mewe <i>et al.</i> model. See Fig. 4.1. . . . .	127
4.4	Theoretical Solar Spectra at 16 MK. Top and middle: New and Old CHIANTI-Coronal Spectra. Bottom: Composite Mewe <i>et al.</i> + CHIANTI-Coronal. . . . .	130
4.5	Two-Temperature Fits Using the Composite Model, With and Without Added Ar . . . . .	131
4.6	May 4 Flare: Actual and Modelled Solar Monitor Output. Solid lines are the sum of 19 gas solar monitor spectra; dashed lines are the sum of the 19 two-temperature models using as input either CHIANTI theoretical solar spectra (top) or the “composite model” (bottom). The mean temperatures quoted here have been weighted by emission measure. . . . .	141
4.7	NEAR X-ray sensor assembly. Figure 7 from Goldsten et al. (1997). . . . .	149

4.8	Detector properties derived from calibration source data for the Al- and Mg-filtered detectors. The plusses represent the Al-filtered values and the diamonds the Mg-filtered values. . . . .	152
4.9	Detector properties derived from calibration source data for the unfiltered detector. The plusses mark the cal-target-derived values and the diamonds the flare-derived values. . . . .	153
4.10	Flare Data from 17 June 2000 . . . . .	155
4.11	Flare Data from 27 December 2000 . . . . .	156
4.12	Theoretical calibration curves for meteoritic material illuminated by a flare from 17 June 2000. Geometry: $\theta_{inc} = 59.3^\circ$ , $\theta_{emiss} = 42.4^\circ$ , $\theta_{phase} = 97.6^\circ$ . . . . .	161
4.13	Temperatures and emission measures vs. time for the May 4, 2000 solar flare. Top: Composite solar model with a “thin-Delrin” model of the graded filter. Bottom: The same composite solar models, but with a thicker-Delrin graded filter. . . . .	165
4.14	May 20 Flare: Actual and Modelled Solar Monitor Output. Solid lines are the sum of 50 gas solar monitor spectra; dashed lines are the sum of the 50 two-temperature models using as input either CHIANTI theoretical solar spectra (top) or the “composite model” (bottom). . . . .	167
4.15	Temperatures and emission measures vs. time for the May 20, 2000 solar flare. . . . .	168
4.16	June 15 Flare: Actual and Modelled Solar Monitor Output. Solid lines are the sum of gas solar monitor spectra; dashed lines are the sum of the two-temperature models using as input either CHIANTI theoretical solar spectra (top) or the “composite model” (bottom). . . . .	170
4.17	June 17 Flare: Actual and Modelled Solar Monitor Output. Solid lines are the sum of 36 gas solar monitor spectra; dashed lines are the sum of the 36 two-temperature models using as input either CHIANTI theoretical solar spectra (top) or the “composite model” (bottom). . . . .	171

4.18	Temperatures, Emission Measures, and GOES Ratios vs. time for the June 17, 2000 solar flare. These data are tabulated as Tables 4.10 and 4.11. . . . .	172
4.19	July 10 Flare: Actual and Modelled Solar Monitor Output. Solid lines are the sum of 75 gas solar monitor spectra; dashed lines are the sum of the 75 two-temperature models using as input the new CHIANTI theoretical solar spectra.	174
4.20	Dec. 27 solar flare. The solid line is the sum of 19 gas solar monitor spectra, corrected for zero shift. The low energy channels are undercounted because of this baseline shift effect. The dashed line is the sum of 19 two-temperature “CHIANTI” models with photospheric solar elemental abundances. . . . .	175
4.21	Dec. 28 solar flare. The solid line is the sum of 17 gas solar monitor spectra, corrected for zero shift. The low energy channels are undercounted because of this baseline shift effect. The dashed line is the sum of 17 two-temperature “CHIANTI” models with photospheric solar elemental abundances. . . . .	176
4.22	Jan. 2 Flare: Actual and Modelled Solar Monitor Output. Solid lines are the sum of 41 gas solar monitor spectra; dashed lines are the sum of the 41 two-temperature models using as input either CHIANTI theoretical solar spectra (top) or the “composite model” (bottom). . . . .	178
4.23	Mg/Si and Al/Si composition ratios for eight flares analyzed using various solar models. Ellipses represent a combination of $1-\sigma$ photon statistical uncertainties and uncertainties due to mineral mixing. . . . .	180
4.24	Composition results for Models 1-7, averaged over eight solar flares. Models 1-4 use the composite solar spectral model and are arranged in order of increasing Delrin-layer thickness. Models 5 and 6 use the 2004 CHIANTI models only and the graded filter models that give the best GOES-ratio match and $\chi^2$ value respectively. The black ellipses represent the “Best Eros” values from Nittler et al. (2001).	181
4.25	Composition results for Models 1-6, averaged over eight solar flares. See Figure 4.24. . . . .	182

4.26 Flare-to-flare variations in Fe/Si composition. Top: Model	
1. Bottom: Model 7. . . . .	183

# **Chapter 4**

## **Results of the XRS Investigation**

### **4.1 Solar Fitting Results**

The free parameters in the fitting of the solar monitor data were the temperatures of the two isothermal components, the relative emission measures of the two components (related to the amounts of hot plasma at each of the two temperatures), the absolute flux received from the flare overall, and the zero shift in the gas proportional counter. Several other parameters were fixed outside the fitting, including the gain and resolution of the detector, the dimensions of the graded filter layers, and the theoretical models of isothermal solar X-ray emission that supplied the input spectra to the fit.

#### **4.1.1 Theoretical Models**

I tested several theoretical models of the isothermal solar X-ray spectrum, produced either by the “MEKAL” code of Mewe et al. (1985) or the newer “CHIANTI” code. Both of these codes have been widely used in the solar X-ray literature (e.g. Peres et al., 2000; Phillips et al., 1999). The inputs to these codes are the set of solar elemental abundances and the plasma temperatures. Mewe et al. use the Meyer (1985) abundances. The CHIANTI (version 4.2) code was run to produce two sets of spectra:



one with the photospheric abundances of Feldman (1992) and one with the coronal abundances, also from Feldman. In all cases, the codes were run to generate spectra at thirty-nine temperatures between 2 and 40 MK.

The spectra generated with the CHIANTI code using solar photospheric elemental abundances generally produced very poor fits (Figure 4.1), particularly at energies lower than 3 keV. (In Figures 4.1-4.3, the dotted lines represent the two isothermal components of the fits. These individual components are on the true energy scale of the X-axis, whereas the data and combined model are frequently zero-shifted because of baseline shifting due to pulse addition in the detector electronics during high count-rate periods, such as flares. See §3.5.2 for a brief discussion of baseline shift.) The CHIANTI 4.2 coronal-abundance spectra were good matches below about 2.5 keV, but poor above 6 keV (Figure 4.2). Several CHIANTI investigators have stated that the 8 keV deficit has been observed independently in RHESSI (Lin et al., 2002) spectra<sup>1</sup> and may be due to the omission<sup>2</sup> of several Fe XXIV dielectronic satellite lines in the current version of the CHIANTI model.

---

<sup>1</sup>“Enrico [Landi] is still trying to work out problems with Fe XXV lines that partly form the 8.2 keV line feature you and we(RHESSI) see – it looks as if some satellite lines were missed out but we’re not sure whether that solves the problem.” (Ken Phillips, 19 August 2004)

<sup>2</sup>“I had a conversation with Enrico yesterday and I think there might be a breakthrough with understanding the too-small intensities of the Fe/Ni 8 keV line feature. He said that addition of some Fe XXIV dielectronic satellite lines which occur in this region, which Chianti has previously left out (as I pointed out in my ApJ paper which came out in April), makes quite a big difference.” (Ken Phillips, 25 August 2004)

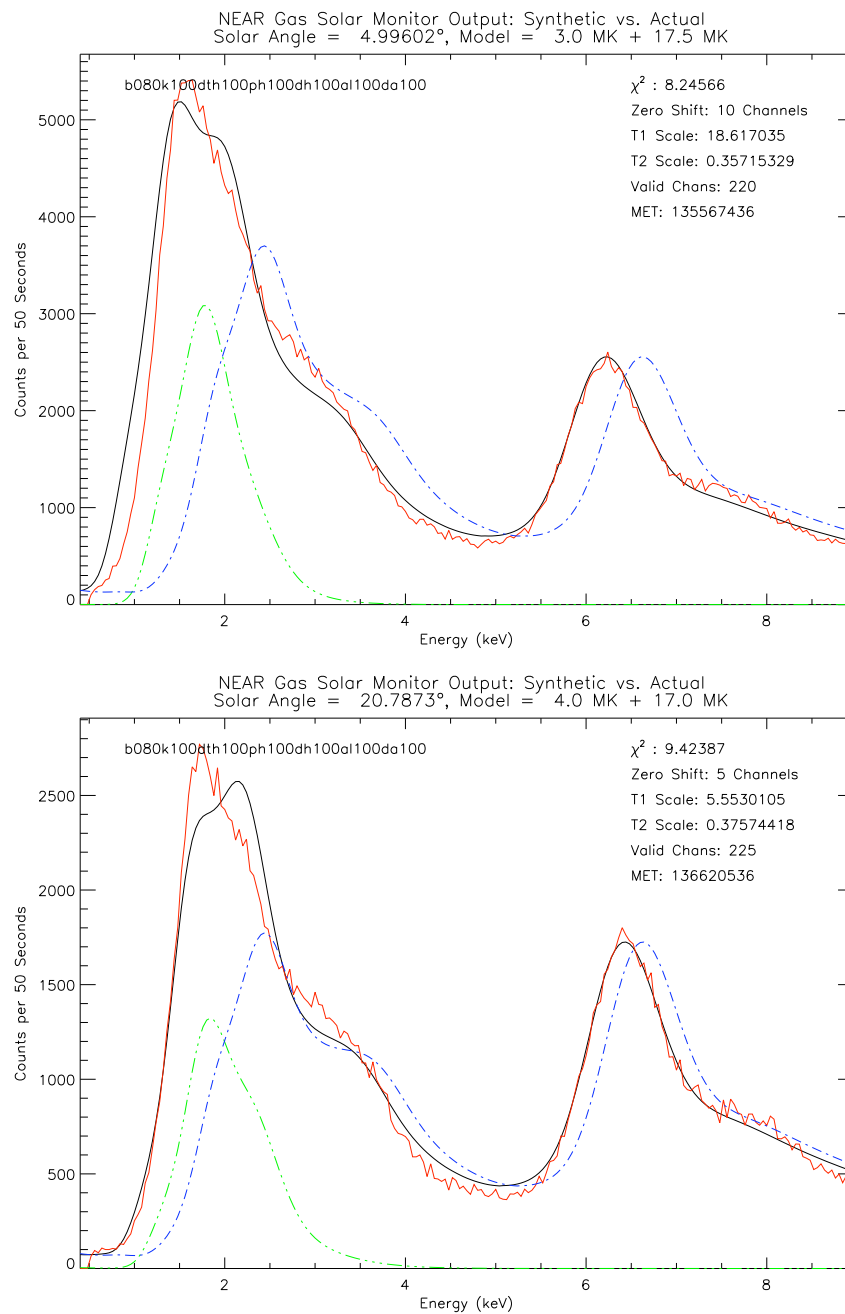


Figure 4.1: Two-Temperature Fits Using CHIANTI-Photospheric Spectra. The dotted lines represent the individual isothermal components of the fit. The solid line is the sum of the two isothermal components, zero-shifted to match the data. The fainter, noisy solid line is the actual spectrum from the gas solar monitor.

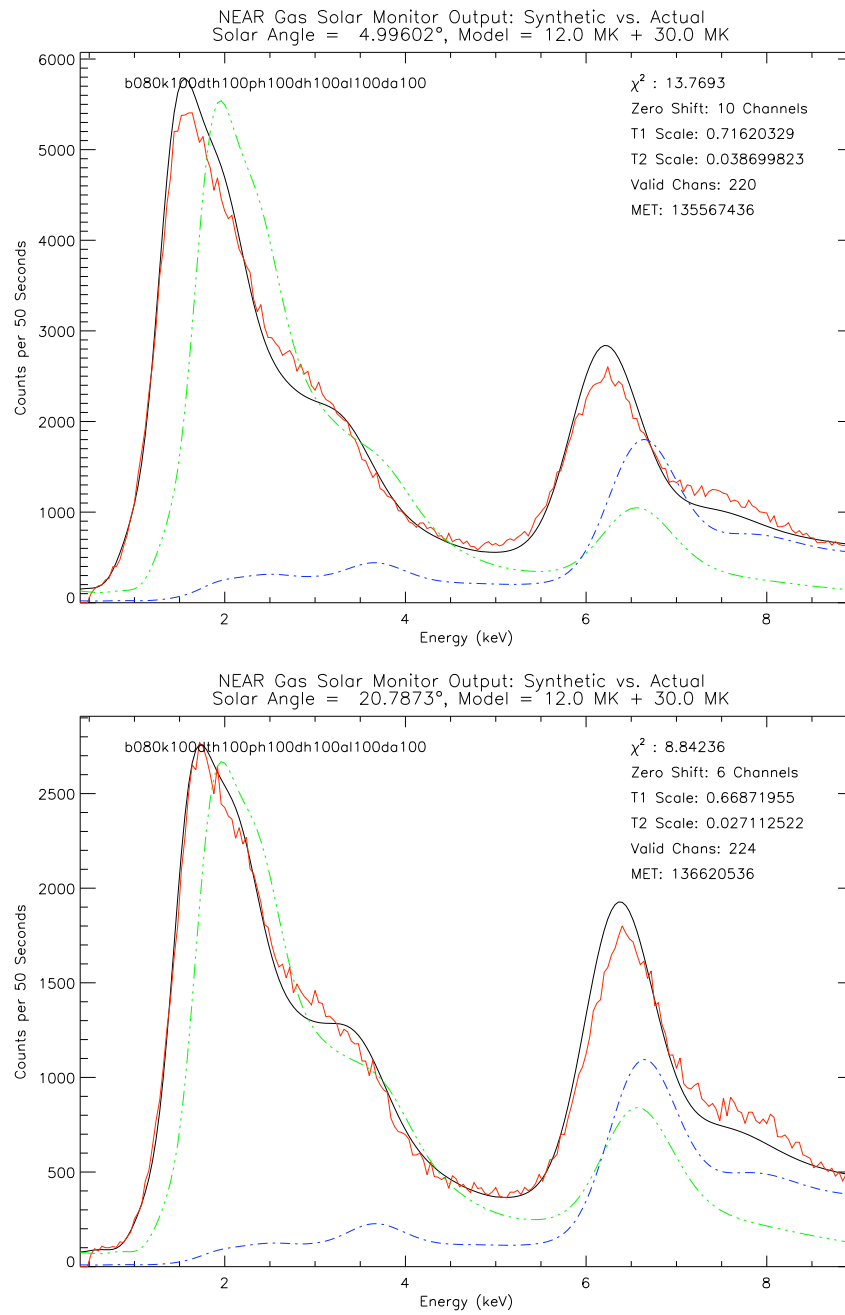


Figure 4.2: Two-Temperature Fits Using CHIANTI-Coronal Spectra. The noisy line is the 50-second solar monitor spectrum; the smooth solid line is the 2003 CHIANTI model. See Fig. 4.1.

### **“Composite” CHIANTI + Mewe *et al.* Models**

At any given temperature, the continua of the Mewe and CHIANTI coronal spectra are nearly identical; only the relative strengths of the lines differed. I constructed a set of composite models (Figure 4.3) in which the spectra below 6 keV (the actual splice was done over the line-free region between 2 and 2.4 Å) were generated by the CHIANTI code and the higher-energy portions by the Mewe *et al.* code.

This composite model has a number of drawbacks. For example, the Mewe code has some known inaccuracies.<sup>3</sup> More importantly, since the low-energy channels are no longer being generated by the same physical model as the high-energy channels, a good fit to the high-energy portion of the spectrum in the high-temperature component of the fit may carry an inaccurate low-energy component. The composite model should be viewed only as an interim solution until the CHIANTI code can be amended.

The composite-model spectra, like the CHIANTI coronal-abundance spectra, also suffer from a persistent deficit in the 3 keV region with

---

<sup>3</sup>“There are certainly some things wrong in Mewe for these lines – some subsidiary Fe XXV lines (“intercombination” lines) are omitted (inclusion of these would make the difference between Chianti and Mewe still wider), the energy/wavelength of one of the lines is wrong in Mewe (line at 8.21 should be 8.30 keV), and the wavelengths of the Ni lines at ~7.75 keV are also wrong. These small problems shouldn’t cause too many problems for the total intensity of the 8 keV feature.”

“The atomic data for these lines in Chianti are based on integration of cross sections, whereas in Mewe (the procedure is based on Mewe *et al.*, 1985, when good atomic data were not widely available) is based on a “g-bar” approximation which has long since been superseded.”

“So in summary Chianti ought to be a better representation of the spectrum than Mewe...” (Ken Phillips, 24 June 2004)

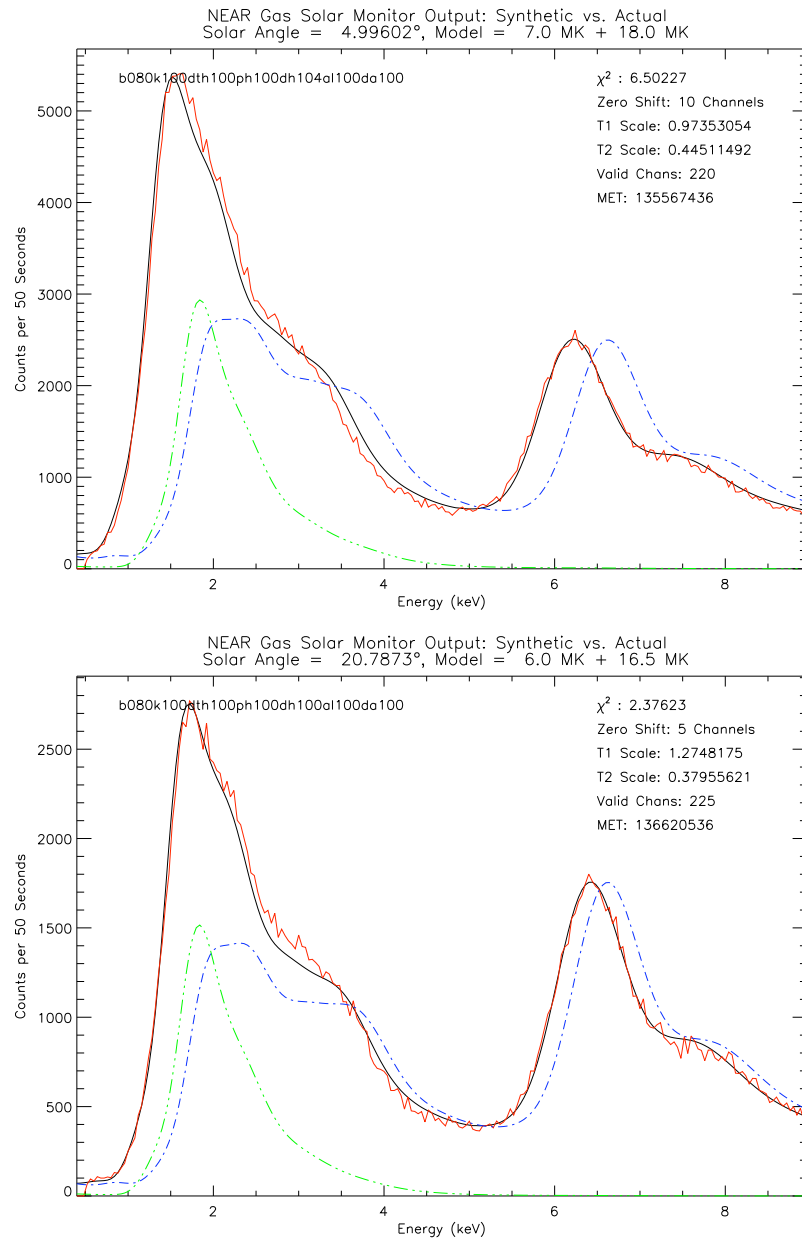


Figure 4.3: Two-Temperature Fits Using Composite Mewe and CHIANTI-Coronal Model Spectra. The noisy line is the 50-second solar monitor spectrum; the smooth solid line is the composite CHIANTI-Coronal + Mewe *et al.* model. See Fig. 4.1.

respect to the NEAR solar monitor data, which cannot be eliminated by any permutation of the graded-filter parameters. The only major elements that produce lines in this region under solar flare conditions are sulfur and argon. Relative to Si and other abundant elements (O, Mg, Fe), the abundances of S and Ar are lower by almost a factor of two in the Feldman (1992) coronal composition than in the Meyer (1985) estimates (see Table 3.2 for the full list of abundances). I experimented with increasing both of these elements until the S/Si and Ar/Si matched those of Meyer (1985). Increasing sulfur in fact worsened the fit because of the other sulfur lines elsewhere in the spectrum; but increasing argon improved it (Figure 4.5). An even better fit was obtained by further increasing Ar abundance to the upper limit of Meyer (1985).

Table 4.1: Solar Element Ratios for Selected Elements: Meyer (1985) vs. Feldman (1992)

	Sources		
	Feldman (1992)	Meyer (1985)	Upper Limit of Meyer (1985)
S/Si	0.15	0.22	
Ar/Si	0.030	0.055	0.177
Ca/Si	0.068	0.076	
Fe/Si	1.0	1.0	

The strength of the 3 keV line itself has a minimal effect on the fluorescence induced in the asteroid, since between it and the K-edges of Mg, Al, Si, and S (Table 3.1) the solar spectrum contains many much stronger emission lines. Since the filter response strongly favors higher-energy lines, the 3 keV line appears much more prominent in the gas solar monitor spectra relative to these lower-energy lines than it is in

reality. However, as is evident from Figure 4.5, its absence can distort the overall fit.

### **Revised CHIANTI Models**

A revised set of CHIANTI-generated theoretical spectra (v. 5.0 pre-release) was provided by Enrico Landi and Ken Phillips (personal communication, 30 September 2004) which included the Fe XXIV dielectronic satellite lines near 8 keV that had previously been omitted from the CHIANTI spectra. Coronal elemental abundances were used to generate these spectra. The new CHIANTI code itself had not, however, yet been released.

The spectra had been generated at integral temperatures between 2 and 40 MK. Spectra were then produced by interpolation at 13.5, 14.5, 15.5, 16.5, 17.5, 18.5, 19.5, 20.5, and 21.5 MK, in order to have the same set of temperatures represented in the fitting process as had been used with the composite Mewe *et al.* + CHIANTI-coronal spectra. I checked these interpolated spectra against the spectra actually generated with the older CHIANTI code at these temperatures and found the continua to be nearly identical.

As will be seen in §4.1.2, the new CHIANTI models fit the solar monitor data much better than the old ones without the Fe XXIV lines, but not as well as the “composite” model in which the channels above 6 keV were fit with the Mewe *et al.* (1985) spectra. The new models also produce

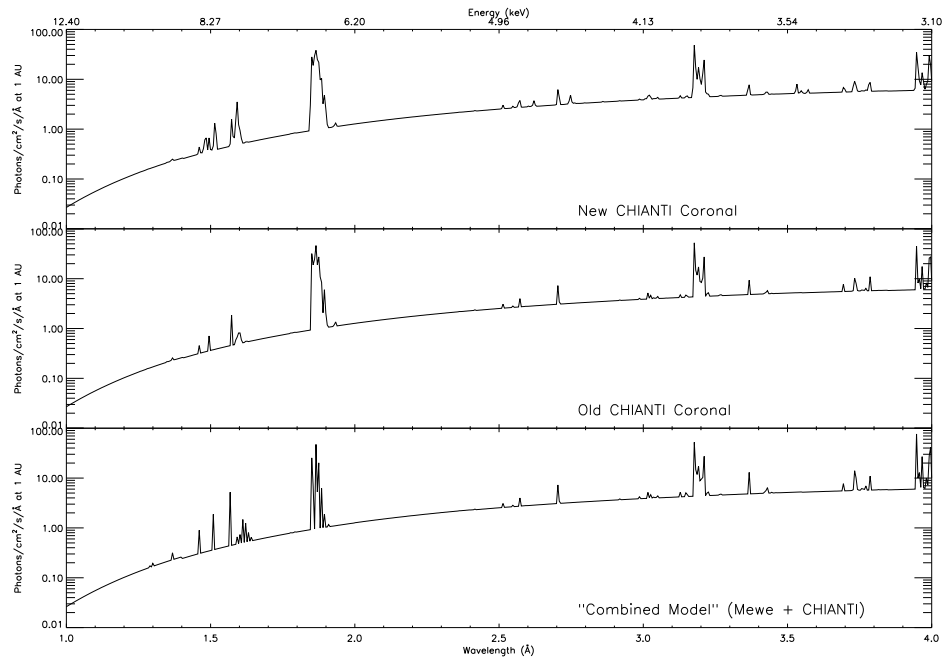
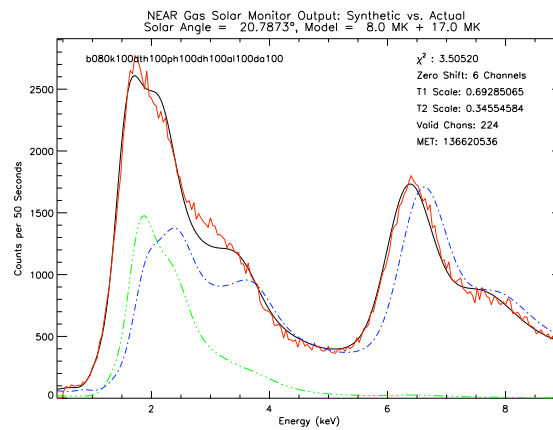


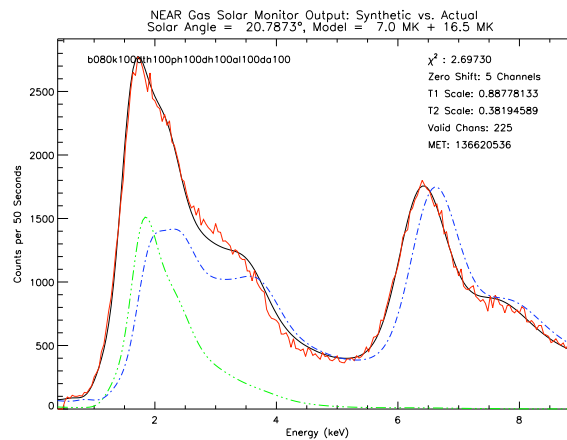
Figure 4.4: Theoretical Solar Spectra at 16 MK. Top and middle: New and Old CHIANTI-Coronal Spectra. Bottom: Composite Mewe *et al.* + CHIANTI-Coronal.

temperatures that are systematically higher than those produced by the composite model, with correspondingly lower emission measures.

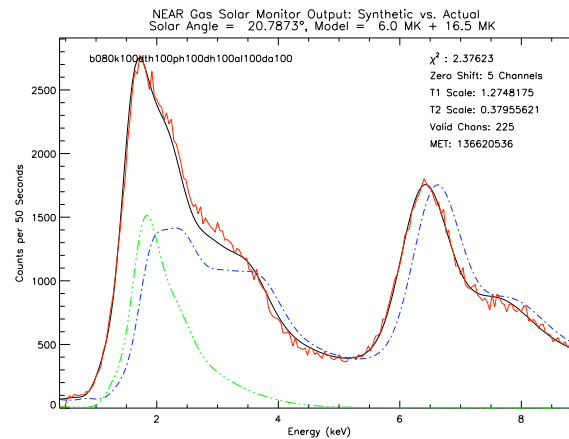




(a) Composite model: Ar from Feldman (1992)



(b) Composite model: Ar/Si from Meyer (1985)



(c) Composite model: Ar/Si at the upper limit of Meyer (1985)

Figure 4.5: Two-Temperature Fits Using the Composite Model, With and Without Added Ar

### 4.1.2 Graded filter characteristics

Tables 4.3 through 4.7 illustrate  $\chi^2$  and GOES comparison results for a series of graded filter models. Tables 4.3, 4.4, and 4.5 use the composite model, in which the spectrum at energies below 6 keV were calculated with the CHIANTI model and energies above 6 keV with the Mewe et al. (1985) model as described in §4.1.1. Tables 4.6 and 4.7 use the new CHIANTI (§4.1.1) model at all energies.

Since the new CHIANTI spectra had been generated using the coronal Ar abundances from Feldman (1992), they produced the same persistent deficits in the 3 keV region as had the CHIANTI v. 4.2 models with these abundances. Because of this, the region between 2.72 and 3.44 keV was eliminated from the  $\chi^2$  fitting. Nevertheless, the  $\chi^2$  values remain consistently higher than those resulting from the composite model.

The  $\chi^2$  results are the medians for fits to 160 solar monitor spectra between May and July 2000. The GOES results are medians for fits to the 56 out of these 160 spectra that were taken between 21 June 2000 and 10 July 2000, when the Earth-orbiting GOES satellite was observing, as nearly as possible, the same face of the Sun as NEAR. (The Earth-Sun-asteroid angle on 21 June was  $16.5^\circ$ , and by 10 July it had decreased to  $5.4^\circ$ . A large solar particle event on 19 July rendered the detectors nearly useless until late August.) The spectra were chosen from data taken during thirteen solar flares of various intensities. They were restricted to flare spectra (as opposed to quiet sun data) in order to sam-

Table 4.2: Solar Monitor Data used in  $\chi^2$  and GOES fitting

MET	Date of First MET (UTC)	Number of Spectra
132825235 - 132826985	2000-May-04 04:37:26	16
135567436 - 135568186	2000-Jun-04 22:20:47	16
135717531 - 135718231	2000-Jun-06 16:02:22	8
136066886 - 136068286	2000-Jun-10 17:04:57	16
136130786 - 136131136	2000-Jun-11 10:49:57	8
136138486 - 136138836	2000-Jun-11 12:58:17	8
136367186 - 136367536	2000-Jun-14 04:29:57	8
136508736 - 136510636	2000-Jun-15 19:49:07	16
136623236 - 136623936	2000-Jun-17 03:37:27	8
137008186 - 137008536	2000-Jun-21 14:33:17	8
137306136 - 137307386	2000-Jun-25 01:19:07	16
137330186 - 137330536	2000-Jun-25 07:59:57	16
137520936 - 137521686	2000-Jun-27 12:59:07	16
137904886 - 137905586	2000-Jul-01 23:38:17	8

ple the entire energy range of the gas solar monitor and to have enough counts in a single spectrum for a reliable fit. They were also selected in order to represent as wide a range as possible of incidence angles of the sun on the graded filter. A list of METs (Mission Elapsed Times) of the samples is given as Table 4.2. (During this period, the integration time of the detector remained constant at 50 s, so each spectrum in Table 4.2 represents 50 seconds of integration.)

It will be immediately apparent from Tables 4.3–4.8 that these three sets of clues are not converging on the same graded-filter model for either set of theoretical solar spectra.

The best  $\chi^2$  in Table 4.3, for example, is produced by the model with the Delrin layer at its nominal thickness but its pinhole diameter at 3% above its specified value; but the model that produces the best match to

Table 4.3: Median  $\chi^2$  for Best Two-Temperature Fits to 160 NEAR Spectra Using Various Graded Filter Models (Composite CHIANTI+MEKAL Models)

Delrin Thickness	Delrin Pinhole Diameter						
	101%	102%	103%	104%	105%	107%	109%
100%	2.29	2.26	2.24	2.26	2.40	2.69	2.80
98%	2.35	2.35	2.29	2.27	2.33	2.62	2.75
96%	2.46	2.40	2.35	2.35	2.34	2.58	2.72
94%	2.62	2.55	2.49	2.43	2.40	2.50	2.68
92%	2.80	2.73	2.65	2.59	2.52	2.47	2.48
90%	2.95	2.88	2.82	2.76	2.68	2.59	2.49

Median RMS GOES Ratio Values for Best Two-Temperature Fits to 56 NEAR Spectra Using Various Graded Filter Models

$$\text{RMS GOES Ratio} = \sqrt{\left[ \frac{(\text{Calculated GOES Ratio}) - (\text{Actual GOES Ratio})}{(\text{Actual GOES Ratio})} \right]^2}$$

Delrin Thickness	Delrin Pinhole Diameter						
	101%	102%	103%	104%	105%	107%	109%
100%	0.065	0.071	0.078	0.082	0.091	0.110	0.130
98%	0.062	0.064	0.066	0.074	0.079	0.098	0.120
96%	0.054	0.057	0.061	0.063	0.065	0.082	0.100
94%	0.061	0.053	0.054	0.056	0.064	0.065	0.085
92%	0.057	0.058	0.056	0.056	0.053	0.064	0.073
90%	0.067	0.051	0.046	0.051	0.053	0.057	0.069

Median RMS GOES LONG Values for Best Two-Temperature Fits to 56 NEAR Spectra Using Various Graded Filter Models

Delrin Thickness	Delrin Pinhole Diameter						
	101%	102%	103%	104%	105%	107%	109%
100%	0.40	0.34	0.31	0.29	0.26	0.22	0.17
98%	0.35	0.34	0.30	0.28	0.25	0.20	0.15
96%	0.33	0.31	0.28	0.26	0.23	0.18	0.14
94%	0.31	0.29	0.26	0.24	0.22	0.17	0.10
92%	0.30	0.28	0.25	0.23	0.20	0.13	0.072
90%	0.28	0.26	0.23	0.18	0.15	0.09	0.041

Table 4.4: Median  $\chi^2$  for Best Two-Temperature Fits to 160 NEAR Spectra Using Various Graded Filter Models (Composite CHIANTI+MEKAL Models)

In these models, the Kapton is 5% thinner than specified and the Be pinhole diameter is 1% larger.

Delrin Thickness	Delrin Pinhole Diameter			
	101%	103%	105%	107%
100%	2.49	2.37	2.41	2.70
98%	2.56	2.46	2.42	2.64
96%	2.76	2.57	2.46	2.60
94%	2.89	2.75	2.57	2.55
92%	3.01	2.91	2.75	2.60
90%	3.18			

Median RMS GOES Ratio Values for Best Two-Temperature Fits to 56 NEAR Spectra Using Various Graded Filter Models

$$\text{RMS GOES Ratio} = \sqrt{\left[ \frac{(\text{Calculated GOES Ratio}) - (\text{Actual GOES Ratio})}{(\text{Actual GOES Ratio})} \right]^2}$$

Delrin Thickness	Delrin Pinhole Diameter			
	101%	103%	105%	107%
100%	0.081	0.096	0.107	0.119
98%	0.066	0.080	0.092	0.106
96%	0.062	0.073	0.076	0.097
94%	0.055	0.063	0.081	0.093
92%	0.053	0.055	0.067	0.084
90%	0.054			

Median RMS GOES LONG Values for Best Two-Temperature Fits to 56 NEAR Spectra Using Various Graded Filter Models

Delrin Thickness	Delrin Pinhole Diameter			
	101%	103%	105%	107%
100%	0.28	0.24	0.19	0.14
98%	0.28	0.22	0.17	0.13
96%	0.26	2.09	0.15	0.11
94%	0.24	0.18	0.14	0.10
92%	0.21	0.16	0.12	0.07
90%	0.20			

Table 4.5: Median  $\chi^2$  for Best Two-Temperature Fits to 160 NEAR Spectra Using Various Graded Filter Models (Composite CHIANTI+MEKAL Models)

In these models, the Kapton layer is 5% thicker than specified.

Delrin Thickness	Delrin Pinhole Diameter						
	99%	100%	101%	103%	105%	107%	109%
100%	2.25	2.29	2.26	2.24	2.36	2.69	2.82
98%	2.34	2.27	2.24	2.25	2.31	2.63	2.82
96%	2.47	2.37	2.31	2.24	2.30	2.57	2.78
94%	2.59	2.50	2.44	2.33	2.30	2.46	2.67
92%	2.77	2.66	2.59	2.45	2.38	2.37	2.44
90%				2.62			

Median RMS GOES Ratio Values for Best Two-Temperature Fits to 56 NEAR Spectra Using Various Graded Filter Models

$$\text{RMS GOES Ratio} = \sqrt{\left[ \frac{(\text{Calculated GOES Ratio}) - (\text{Actual GOES Ratio})}{(\text{Actual GOES Ratio})} \right]^2}$$

Delrin Thickness	Delrin Pinhole Diameter						
	99%	100%	101%	103%	105%	107%	109%
100%	0.067	0.066	0.065	0.077	0.071	0.067	0.084
98%	0.054	0.058	0.057	0.061	0.073	0.065	0.074
96%	0.064	0.049	0.049	0.048	0.055	0.063	0.070
94%	0.085	0.064	0.052	0.045	0.045	0.052	0.061
92%	0.102	0.088	0.073	0.050	0.037	0.040	0.053
90%				0.068			

Median RMS GOES LONG Values for Best Two-Temperature Fits to 56 NEAR Spectra Using Various Graded Filter Models

Delrin Thickness	Delrin Pinhole Diameter						
	99%	100%	101%	103%	105%	107%	109%
100%	0.52	0.48	0.45	0.39	0.34	0.29	0.24
98%	0.50	0.46	0.43	0.37	0.32	0.27	0.22
96%	0.49	0.44	0.41	0.35	0.30	0.25	0.19
94%	0.46	0.42	0.39	0.34	0.29	0.22	0.15
92%	0.44	0.40	0.38	0.32	0.26	0.18	0.12
90%				0.30			

Table 4.6: Median  $\chi^2$  for Best Two-Temperature Fits to 160 NEAR Spectra Using Various Graded Filter Models (New CHIANTI Models)

In these models, the graded filter dimensions other than Delrin thickness and Delrin pinhole diameter are all as originally specified.

Delrin Thickness	Delrin Pinhole Diameter						
	99%	100%	101%	103%	105%	107%	109%
104	3.17	3.15	3.15	3.17	3.24	3.31	3.39
102	3.29	3.27	3.26	3.24	3.23	3.28	3.36
100	3.39	3.37	3.36	3.34	3.32	3.31	3.33
98	3.53	3.52	3.49	3.49	3.49	3.47	3.46
96							3.62

Median RMS GOES Ratio Values for Best Two-Temperature Fits to 56 NEAR Spectra Using Various Graded Filter Models

$$\text{RMS GOES Ratio} = \sqrt{\left[ \frac{(\text{Calculated GOES Ratio}) - (\text{Actual GOES Ratio})}{(\text{Actual GOES Ratio})} \right]^2}$$

Delrin Thickness	Delrin Pinhole Diameter						
	99%	100%	101%	103%	105%	107%	109%
104	0.068	0.069	0.071	0.058	0.079	0.080	0.080
102	0.065	0.062	0.067	0.062	0.047	0.074	0.073
100	0.075	0.068	0.066	0.070	0.054	0.046	0.074
98	0.083	0.082	0.077	0.066	0.067	0.057	0.050
96							0.057

Median RMS GOES LONG Values for Best Two-Temperature Fits to 56 NEAR Spectra Using Various Graded Filter Models

Delrin Thickness	Delrin Pinhole Diameter						
	99%	100%	101%	103%	105%	107%	109%
104	0.46	0.43	0.40	0.34	0.29	0.23	0.189
102	0.45	0.41	0.38	0.32	0.27	0.22	0.174
100	0.43	0.41	0.36	0.30	0.25	0.20	0.158
98	0.41	0.38	0.36	0.29	0.23	0.18	0.147
96							0.132

Table 4.7: Median  $\chi^2$  for Best Two-Temperature Fits to 160 NEAR Spectra Using Various Graded Filter Models (New CHIANTI Models)

In these models, the aluminum layer is 10% thicker than specified.

Delrin Thickness	Delrin Pinhole Diameter						
	99%	100%	101%	103%	105%	107%	109%
104	3.01	3.04	3.02	3.02	3.03	3.10	3.17
102	3.16	3.15	3.11	3.08	3.08	3.08	3.13
100	3.30	3.27	3.22	3.19	3.17	3.17	3.17
98	3.52	3.48	3.43	3.39	3.37	3.36	

Median RMS GOES Ratio Values for Best Two-Temperature Fits to 56 NEAR Spectra Using Various Graded Filter Models

$$\text{RMS GOES Ratio} = \sqrt{\left[ \frac{(\text{Calculated GOES Ratio}) - (\text{Actual GOES Ratio})}{(\text{Actual GOES Ratio})} \right]^2}$$

Delrin Thickness	Delrin Pinhole Diameter						
	99%	100%	101%	103%	105%	107%	109%
104	0.065	0.072	0.072	0.065	0.061	0.074	0.082
102	0.068	0.069	0.069	0.069	0.051	0.056	0.076
100	0.080	0.073	0.071	0.070	0.058	0.049	0.060
98	0.082	0.084	0.080	0.073	0.064	0.059	

Median RMS GOES LONG Values for Best Two-Temperature Fits to 56 NEAR Spectra Using Various Graded Filter Models

Delrin Thickness	Delrin Pinhole Diameter						
	99%	100%	101%	103%	105%	107%	109%
104	0.47	0.42	0.40	0.34	0.29	0.24	0.19
102	0.43	0.41	0.39	0.32	0.26	0.22	0.17
100	0.43	0.41	0.35	0.30	0.25	0.20	0.16
98	0.41	0.38	0.35	0.29	0.24	0.18	



Table 4.8: Median  $\chi^2$  for Best Two-Temperature Fits to 160 NEAR Spectra Using Various Graded Filter Models (New CHIANTI Models)

In these models, all graded filter parameters other than Delrin thickness, aluminum thickness, and Delrin pinhole diameter are as originally specified.

Delrin Pinhole Diam. 107%					Delrin Pinhole Diam. 100%				
Delrin Thickness	Aluminum Thickness				Delrin Thickness	Aluminum Thickness			
	95%	100%	105%	110%		95%	100%	105%	110%
104%	3.43	3.31	3.21	3.10	104%	3.22	3.15	3.09	3.04
102%	3.41	3.28	3.18	3.08	102%	3.33	3.27	3.21	3.15
100%	3.40	3.31	3.25	3.17	100%	3.42	3.37	3.31	3.27
98%	3.54	3.47	3.41	3.36	98%	3.51	3.52	3.49	3.48

Median RMS GOES Ratio Values for Best Two-Temperature Fits to 56 NEAR Spectra Using Various Graded Filter Models

$$\text{RMS GOES Ratio} = \sqrt{\left[ \frac{(\text{Calculated GOES Ratio}) - (\text{Actual GOES Ratio})}{(\text{Actual GOES Ratio})} \right]^2}$$

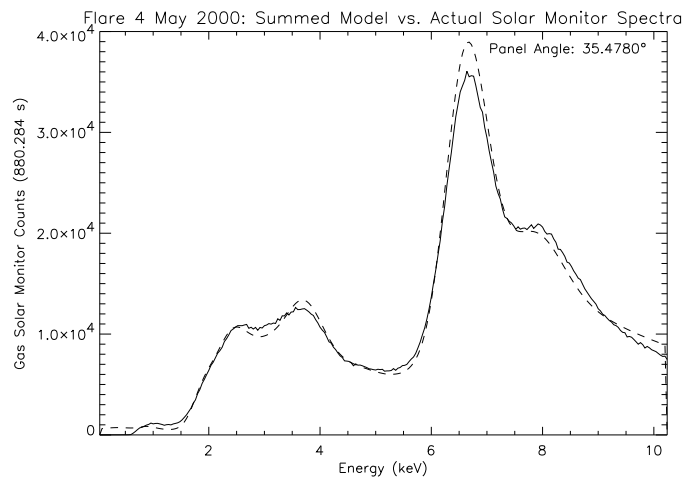
Delrin Pinhole Diam. 107%					Delrin Pinhole Diam. 100%				
Delrin Thickness	Aluminum Thickness				Delrin Thickness	Aluminum Thickness			
	95%	100%	105%	110%		95%	100%	105%	110%
104%	0.079	0.080	0.081	0.074	104%	0.069	0.069	0.071	0.072
102%	0.077	0.074	0.054	0.056	102%	0.064	0.065	0.069	0.069
100%	0.061	0.046	0.047	0.049	100%	0.067	0.068	0.070	0.073
98%	0.055	0.057	0.059	0.059	98%	0.081	0.082	0.083	0.084

Median RMS GOES LONG Values for Best Two-Temperature Fits to 56 NEAR Spectra Using Various Graded Filter Models

Delrin Pinhole Diam. 107%					Delrin Pinhole Diam. 100%				
Delrin Thickness	Aluminum Thickness				Delrin Thickness	Aluminum Thickness			
	95%	100%	105%	110%		95%	100%	105%	110%
104%	0.230	0.232	0.235	0.239	104%	0.432	0.433	0.428	0.419
102%	0.218	0.217	0.219	0.221	102%	0.403	0.405	0.403	0.405
100%	0.201	0.203	0.206	0.201	100%	0.400	0.407	0.401	0.407
98%	0.186	0.184	0.182	0.184	98%	0.377	0.383	0.383	0.383

the GOES channel ratios (Delrin thickness 90%, Delrin pinhole diameter 103%) has the second-poorest  $\chi^2$  in the grid. Meanwhile, the match to the GOES absolute flux in the long-wavelength channel is best when the graded filter is made least attenuating, whether by enlarged pinholes or thin layers, suggesting that the GOES absolute flux is measuring a “fainter” Sun than can easily be derived from the NEAR data. Since the accuracy of the GOES absolute calibration is uncertain, I have considered the GOES channel ratios to be a more reliable guide to the quality of the graded filter model than the absolute flux measurements.

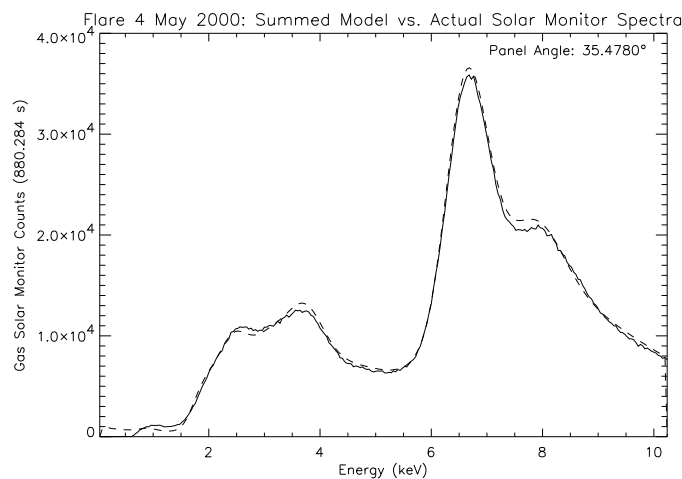
In contrast to the composite model, the new CHIANTI models give the best  $\chi^2$  results when the graded filter model has thicker Delrin and aluminum layers than specified — that is, when it is assumed to be more attenuating at high energies. This can be observed most clearly in Table 4.8, in which the Delrin and aluminum thicknesses are varied for two different values of the Delrin pinhole diameter. The bottom portions of Tables 4.6–4.8 also show, however, that as with the composite theoretical models, the absolute flux of the GOES-Long flux agrees best with the models when the filter is as thin as possible. The best match to the GOES channel ratios, however, does not coincide with either of these extremes. The minimum RMS GOES ratio value occurs when the Delrin and aluminum layers are at their nominal thicknesses and the Delrin pinhole diameter is 7% larger than originally specified.



(a) New CHIANTI Theoretical Spectra:

Mean High-Temperature Component: 25.5 MK ( $EM=0.157 \cdot 10^{49} \text{ cm}^{-3}$ )

Mean Low-Temperature Component: 11.5 MK ( $EM=3.6 \cdot 10^{49} \text{ cm}^{-3}$ )



(b) Composite Mewe + CHIANTI Spectra with Ar/Si from Meyer (1985):

Mean High-Temperature Component: 17.3 MK ( $EM=0.9 \cdot 10^{49} \text{ cm}^{-3}$ )

Mean Low-Temperature Component: 9.2 MK ( $EM=3.7 \cdot 10^{49} \text{ cm}^{-3}$ )

Figure 4.6: May 4 Flare: Actual and Modelled Solar Monitor Output. Solid lines are the sum of 19 gas solar monitor spectra; dashed lines are the sum of the 19 two-temperature models using as input either CHIANTI theoretical solar spectra (top) or the “composite model” (bottom). The mean temperatures quoted here have been weighted by emission measure.

### 4.1.3 Model Selection and Comparison

Six graded-filter models were selected for use in the asteroid-fluorescence data analysis. Models 1–4 performed well on the 160-spectrum test sample with the composite CHIANTI-coronal + Mewe et al. solar models. Models 5 and 6 were the result of testing the sample spectra with the revised CHIANTI models.

“Model 1” is the least attenuating model, and the one with the overall best RMS match to the GOES ratios. It has a Delrin-layer thickness 92% of the specified value and a Delrin pinhole 5% broader in diameter. However, the Kapton layer is 5% thicker than specified. When paired with the composite solar spectral models, this model produced a  $\chi^2$  value of 2.38 and an RMS GOES ratio of 0.037. This model is in Table 4.5, where it can be seen that a 2% change in the Delrin thickness or Delrin pinhole diameter worsens the GOES match, although increasing the Delrin thickness would improve the  $\chi^2$  median.

Models 2 and 3 are compromises between the  $\chi^2$  match to the solar monitor data itself and good modelling of the GOES ratios. They both have very similar  $\chi^2$  and GOES RMS values, although Model 3 is considerably more attenuating than Model 2, particularly at steep solar panel angles.

When used with the composite theoretical spectra, Model 4 produced a better  $\chi^2$  match to the solar monitor data itself than any other model

that has been tested. Its RMS GOES value, however, is worse than those of Models 1–3.

Model 5 produces the best RMS GOES match of any graded filter model when tested against the revised CHIANTI-coronal spectra.

Model 6 produces the best  $\chi^2$  of the CHIANTI-coronal models tested.

#### **4.1.4 An Example of Solar Flare Fitting**

Sample results of fitting flare data from the solar monitor are given as Tables 4.10 and 4.11. MET is the mission elapsed time, in seconds, of each individual 50-second spectrum. T1 and T2 are the temperatures of the two components of the fit, in MK; EM1 and EM2 are the corresponding emission measures, in  $10^{49} \text{ cm}^{-3}$ .

“Model GOES Ratio” is the result of putting the two-temperature fitted spectrum through the response functions of the two GOES-8 channels, then dividing the short-wavelength output by the long-wavelength output. In general, for an isothermal spectrum, this ratio increases with increasing temperature. “Model GOES-L” and “Model GOES-S” are the modelled outputs of each GOES channel individually. The units are  $\text{W/m}^2$ . The GOES instruments do not actually measure  $\text{W/m}^2$ ; they provide current in amperes, which is converted to  $\text{W/m}^2$  via a wavelength-averaged transfer function before being recorded in the SOLARSOFT database. Here I have multiplied the model solar spectrum by the true

Table 4.9: Selected Graded Filter Models. All percentages refer to changes from the specified dimensions in Table 3.4.

Model	Delrin Thickness	Del. Pinhole Diameter	Other	$\chi^2$	RMS GOES Ratio	RMS GOES Long
Composite Models						
1	92%	105%	Kap. 105%	2.38	0.037	0.26
2	94%	103%	Be Pin. 99%	2.44	0.052	0.28
3	96%	101%	—	2.46	0.054	0.33
4	100%	105%	Be Pin. 99%, Del. Dens. 98%	2.23	0.071	0.27
New CHIANTI Models						
5	100%	107%	—	3.35	0.045	0.196
7	102%	105%	Al Thick. 105%	3.16	0.049	
6	104%	99%	Al Thick. 110%	3.01	0.065	0.47
8	100%	100%	—	3.37	0.068	

Table 4.10: Solar Fitting Results for a Flare (2000-June-17): Composite Model

The graded-filter model used for this fit had the Kapton layer at 105% of specified thickness; the Delrin layer at 92%, and the Delrin pinhole at 105% of the specified diameter.

MET	T1	T2	EM1	EM2	Model GOES Ratio	Model GOES-L	Model GOES-S	Real GOES Ratio	Real GOES-L	Real GOES-S	Real GOES EM	$\chi^2$	$\chi^2$ -hi
136620036	6	18.5	2.96	1.18	0.155	5.26e-05	8.14e-06	0.194	3.48e-05	6.73e-06	3.806	8.268	4.091
136620086	8	18.5	1.65	1.03	0.155	4.9e-05	7.62e-06	0.181	3.37e-05	6.1e-06	3.834	5.511	1.646
136620136	8	18.5	1.94	0.92	0.143	4.91e-05	7e-06	0.172	3.21e-05	5.51e-06	3.779	4.602	2.358
136620186	8	18.5	2.03	0.82	0.136	4.75e-05	6.43e-06	0.164	2.99e-05	4.9e-06	3.625	4.19	2.651
136620236	8	18.5	1.99	0.73	0.13	4.42e-05	5.76e-06	0.158	2.69e-05	4.24e-06	3.336	3.914	1.643
136620286	7	18	2.48	0.70	0.12	4.23e-05	5.06e-06	0.157	2.43e-05	3.8e-06	3.021	3.033	1.965
136620336	7	18	2.24	0.64	0.12	3.82e-05	4.58e-06	0.158	2.14e-05	3.38e-06	2.657	3.297	2.157
136620386	7	18	2.13	0.54	0.115	3.45e-05	3.97e-06	0.159	1.92e-05	3.05e-06	2.371	2.753	1.662
136620436	7	17.5	1.90	0.51	0.112	3.14e-05	3.52e-06	0.16	1.7e-05	2.72e-06	2.094	2.31	1.329
136620486	8	18	1.40	0.40	0.115	2.78e-05	3.2e-06	0.161	1.55e-05	2.5e-06	1.895	2.635	1.264
136620536	7	17.5	1.66	0.42	0.109	2.66e-05	2.91e-06	0.167	1.45e-05	2.42e-06	1.737	2.214	1.454
136620586	7	17.5	1.44	0.42	0.116	2.47e-05	2.86e-06	0.172	1.36e-05	2.34e-06	1.596	2.214	1.416
136620636	7	17.5	1.34	0.41	0.117	2.34e-05	2.74e-06	0.174	1.31e-05	2.27e-06	1.531	2.364	1.362
136620686	7	17	1.21	0.43	0.119	2.26e-05	2.7e-06	0.171	1.28e-05	2.18e-06	1.505	2.306	1.748
136620736	7	17	1.28	0.39	0.113	2.24e-05	2.54e-06	0.165	1.24e-05	2.04e-06	1.497	2.527	1.356
136620786	7	16	1.14	0.43	0.11	2.17e-05	2.39e-06	0.158	1.21e-05	1.91e-06	1.497	2.289	1.717
136620836	8	16	0.92	0.38	0.109	2.08e-05	2.27e-06	0.15	1.2e-05	1.79e-06	1.53	2.062	1.411
136620886	9	16.5	0.88	0.28	0.106	2.01e-05	2.13e-06	0.138	1.21e-05	1.66e-06	1.625	2.164	1.495
136620936	10	17.5	0.89	0.17	0.103	1.97e-05	2.03e-06	0.129	1.2e-05	1.55e-06	1.687	2.645	1.978
136620986	9	16.5	0.99	0.20	0.093	1.97e-05	1.82e-06	0.122	1.18e-05	1.43e-06	1.713	2.466	1.361
136621036	10	18	0.93	0.10	0.093	1.86e-05	1.74e-06	0.116	1.16e-05	1.35e-06	1.732	2.31	1.276
136621086	9	16	0.94	0.17	0.087	1.82e-05	1.59e-06	0.11	1.13e-05	1.25e-06	1.745	1.903	1.157
136621136	10	17.5	0.85	0.09	0.09	1.69e-05	1.52e-06	0.106	1.1e-05	1.16e-06	1.749	1.842	1.505
136621186	10	18.5	0.84	0.06	0.087	1.6e-05	1.4e-06	0.103	1.08e-05	1.11e-06	1.761	1.836	1.234
136621236	10	20	0.85	0.05	0.086	1.56e-05	1.34e-06	0.101	1.06e-05	1.07e-06	1.75	2.173	1.526
136621286	9	17.5	0.94	0.09	0.079	1.63e-05	1.27e-06	0.098	1.04e-05	1.02e-06	1.745	1.932	1.202
136621336	9	17	0.89	0.09	0.08	1.53e-05	1.22e-06	0.095	1.02e-05	9.72e-07	1.757	1.854	1.195
136621386	9	17	0.91	0.08	0.077	1.53e-05	1.18e-06	0.092	1e-05	9.26e-07	1.75	2.413	1.372
136621436	9	18	0.92	0.06	0.075	1.5e-05	1.12e-06	0.092	9.89e-06	9.08e-07	1.735	1.89	1.13
136621486	9	17	0.87	0.08	0.076	1.47e-05	1.12e-06	0.092	9.85e-06	9.06e-07	1.726	1.893	1.277
136621536	9	17.5	0.87	0.07	0.077	1.45e-05	1.11e-06	0.094	9.71e-06	9.12e-07	1.677	2.324	1.469
136621586	9	18.5	0.86	0.07	0.078	1.43e-05	1.12e-06	0.095	9.54e-06	9.08e-07	1.631	1.957	1.143
136621636	8	17	0.99	0.10	0.073	1.45e-05	1.06e-06	0.097	9.4e-06	9.13e-07	1.587	1.869	1.036
136621686	9	18.5	0.83	0.07	0.081	1.41e-05	1.14e-06	0.096	9.18e-06	8.68e-07	1.556	2.134	1.076
136621736	9	19	0.82	0.06	0.08	1.37e-05	1.1e-06	0.096	9.01e-06	8.86e-07	1.528	2.088	1.424
136621786	9	18.5	0.80	0.07	0.081	1.34e-05	1.09e-06	0.095	8.78e-06	8.36e-07	1.5	1.971	1.138

Table 4.1.1: Solar Fitting Results for a Flare (2000-June-17): New CHIANTI Coronal

The graded-filter model used for this fit had the Be pinhole at 101% of the specified diameter and the Delrin pinhole at 107%.

MET	T1	T2	EM1	EM2	Model GOES-L	Model GOES-S	Real GOES Ratio	Real GOES-L	Real GOES-S	Real GOES EM	$\chi^2$	$\chi^2$ -hi
136620032	12.0	25.0	1.73	0.35	4.88e-05	8.43e-06	0.194	3.48e-05	6.73e-06	3.806	15.895	13.689
136620080	12.0	25.0	1.78	0.30	4.80e-05	7.84e-06	0.181	3.37e-05	6.10e-06	3.834	9.954	11.208
136620128	12.0	26.0	1.82	0.23	4.68e-05	7.28e-06	0.172	3.21e-05	5.51e-06	3.779	8.824	9.664
136620192	12.0	26.0	1.73	0.21	4.40e-05	6.71e-06	0.164	2.99e-05	4.90e-06	3.625	8.513	10.743
136620240	12.0	26.0	1.70	0.18	4.22e-05	6.18e-06	0.158	2.69e-05	4.24e-06	3.336	7.167	9.147
136620288	12.0	26.0	1.58	0.15	3.88e-05	5.57e-06	0.157	2.43e-05	3.80e-06	3.021	7.168	9.072
136620336	11.0	24.0	1.51	0.20	3.55e-05	4.86e-06	0.158	2.14e-05	3.38e-06	2.657	5.873	7.626
136620384	11.0	24.0	1.37	0.17	3.19e-05	4.26e-06	0.159	1.92e-05	3.05e-06	2.371	5.204	5.962
136620432	11.0	24.0	1.24	0.14	2.86e-05	3.73e-06	0.160	1.70e-05	2.72e-06	2.094	5.176	6.467
136620480	11.0	24.0	1.16	0.12	2.64e-05	3.37e-06	0.161	1.55e-05	2.50e-06	1.895	4.543	4.883
136620544	11.0	24.0	1.08	0.11	2.45e-05	3.13e-06	0.167	1.45e-05	2.42e-06	1.737	4.531	5.847
136620592	11.0	24.0	0.98	0.12	2.28e-05	3.02e-06	0.172	1.36e-05	2.34e-06	1.596	4.453	6.067
136620640	10.0	21.5	1.01	0.17	2.25e-05	2.86e-06	0.174	1.31e-05	2.27e-06	1.531	5.194	5.138
136620688	11.0	23.0	0.92	0.12	2.15e-05	2.84e-06	0.171	1.28e-05	2.18e-06	1.505	4.715	5.460
136620736	11.0	22.0	0.88	0.13	2.09e-05	2.73e-06	0.165	1.24e-05	2.04e-06	1.497	4.168	5.164
136620784	11.0	21.0	0.85	0.12	2.01e-05	2.52e-06	0.158	1.21e-05	1.91e-06	1.497	4.315	5.630
136620832	11.0	21.5	0.88	0.10	1.98e-05	2.36e-06	0.150	1.20e-05	1.79e-06	1.530	3.846	4.009
136620880	11.0	21.0	0.88	0.09	1.94e-05	2.22e-06	0.138	1.21e-05	1.66e-06	1.625	3.318	3.535
136620928	11.0	21.5	0.89	0.07	1.91e-05	2.07e-06	0.129	1.20e-05	1.55e-06	1.687	3.484	3.812
136620992	11.0	21.5	0.89	0.05	1.86e-05	1.94e-06	0.122	1.18e-05	1.43e-06	1.713	3.114	3.504
136621040	11.0	23.0	0.88	0.04	1.79e-05	1.79e-06	0.116	1.16e-05	1.35e-06	1.732	3.109	2.472
136621088	11.0	21.5	0.84	0.04	1.72e-05	1.71e-06	0.110	1.13e-05	1.25e-06	1.745	2.482	2.407
136621136	11.0	22.0	0.83	0.03	1.68e-05	1.62e-06	0.106	1.10e-05	1.16e-06	1.749	2.191	2.054
136621184	11.0	25.0	0.81	0.02	1.60e-05	1.51e-06	0.103	1.08e-05	1.11e-06	1.761	2.087	1.691
136621232	11.0	26.0	0.79	0.01	1.56e-05	1.45e-06	0.101	1.06e-05	1.07e-06	1.750	2.433	2.006
136621280	10.0	20.5	0.85	0.04	1.56e-05	1.34e-06	0.098	1.02e-05	1.02e-06	1.745	2.195	1.922
136621344	10.0	20.5	0.83	0.04	1.51e-05	1.29e-06	0.095	1.02e-05	9.72e-07	1.757	1.973	1.701
136621392	10.0	20.0	0.81	0.04	1.47e-05	1.23e-06	0.092	1.00e-05	9.26e-07	1.750	3.004	2.414
136621440	10.0	22.0	0.81	0.03	1.44e-05	1.18e-06	0.092	9.89e-06	9.08e-07	1.735	2.196	1.996
136621488	10.0	21.5	0.79	0.03	1.42e-05	1.17e-06	0.092	9.85e-06	9.06e-07	1.726	2.008	1.605
136621536	10.0	22.0	0.79	0.03	1.37e-05	1.17e-06	0.094	9.71e-06	9.12e-07	1.677	2.469	1.939
136621584	10.0	23.0	0.76	0.03	1.37e-05	1.17e-06	0.095	9.54e-06	9.08e-07	1.631	2.173	1.709
136621632	10.0	24.0	0.77	0.03	1.39e-05	1.18e-06	0.097	9.40e-06	9.13e-07	1.587	2.172	1.728
136621680	10.0	23.0	0.74	0.03	1.34e-05	1.17e-06	0.096	9.18e-06	8.86e-07	1.556	2.531	1.814
136621728	10.0	23.0	0.73	0.03	1.32e-05	1.15e-06	0.096	9.01e-06	8.68e-07	1.528	2.387	2.046
136621792	10.0	22.0	0.71	0.03	1.30e-05	1.13e-06	0.095	8.78e-06	8.36e-07	1.500	2.379	1.808



spectral transfer function in order to model the GOES output in amps, then multiplied by the wavelength-averaged transfer function in order to reproduce the same units of  $\text{W/m}^2$ . “Real GOES Ratio,” “Real GOES-L,” and “Real GOES-S” are the same quantities from the SOLARSOFT database, averaged over the 50-second NEAR integration periods. “Real GOES-EM” is the GOES emission measure estimate from the SOLARSOFT database, calculated by using the models of Garcia (1994). Note that these emission measures were derived by assuming the solar flares are isothermal and modelling their spectra according to Mewe et al. (1985), so they are not directly comparable to our emission measures.  $\chi^2$  is the reduced  $\chi^2$  value of the two-temperature fit. In the case of the new CHIANTI-coronal models, channels between 2.72 and 3.44 keV are not included in this  $\chi^2$  value. Channels with fewer than 5 counts in either the data or the model spectra were also eliminated from the fitting for all models. “ $\chi^2$ -high” is the  $\chi^2$  value calculated only for channels above 5.6 keV.

## **4.2 Interpreting the Asteroid-Pointing Data**

### **4.2.1 Calibration with the Calibration Sources**

In order to monitor the gain, zero, and resolution of the asteroid-pointing detectors, the NEAR XRS included three radioactive Fe-55 calibration sources for use with the asteroid-pointing proportional coun-

ters, each of which could be rotated into and out of the field of view of one detector. (See Figure 4.7 for a diagram of the detector assembly, including the calibration rod.) The Fe-55 sources emitted X-rays in the Mn  $K_\alpha$  (88%) and  $K_\beta$  (12%) lines at 5.898 and 6.490 keV respectively. The detectors also registered escape peaks for the two lines at 2.941 and 3.533 keV.

The detectors' response to the pair of monoenergetic lines received from the Fe-55 source was modelled and fit to the calibration data. The free parameters in the fit were the source strength, detector gain, detector zero, and resolution. Resolution was represented by the "FWHM parameter," when:

$$FWHM(E) = FWHM \text{ Parameter} \cdot E^{1/2} \quad (4.1)$$

A Gaussian shape was assumed for all four peaks. The scale of the cosmic-ray background, whose shape was established by calibration-source- and asteroid- free data taken within 24 hours of the calibration data, was also allowed to float, but usually remained within 1% (and always within 2%, for the two filtered detectors) of simple scaling by live time.

Calibration source fitting results are summarized in Table 4.12 and Figures 4.8 and 4.9.

The Fe-55 source for the unfiltered detector was much weaker than the other two sources, and the statistics on its calibration data were poor. Because of this, the error bars on its gain, zero, and FWHM in Ta-

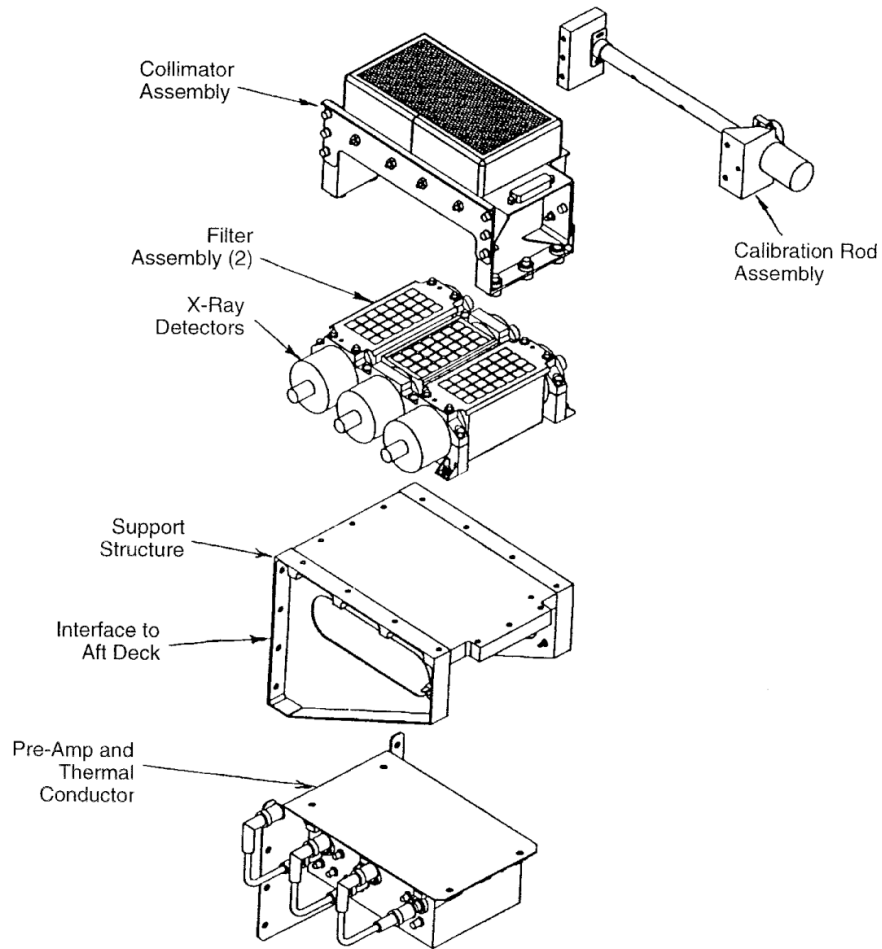


Figure 4.7: NEAR X-ray sensor assembly. Figure 7 from Goldsten et al. (1997).

ble 4.12 are much higher than those derived for the other two detectors. The unfiltered detector, however, had the best statistics of the three in the asteroid fluorescence during the solar flares themselves, and more precise detector characteristics could be derived from the flare spectra (Table 4.13). In the Mg- and Al-filtered detectors, however, much better statistics were derived from the calibration source data than from flare data.

The resolution was the most variable of the detector characteristics. It became degraded whenever the instrument was shut off, as in safe mode, and took several weeks to approach its limit (FWHM Parameter = 0.340). This can be observed in Table 4.12, as the resolutions of the Al and Mg detectors improve slowly from April to late May. At some point between May 24 and May 30 (Days 145-151 in Figure 4.8) the resolution was degraded again, after which the detectors began another slow recovery.

No calibration data were taken between 9 June 2000 and 7 August 2000.

#### **4.2.2 Extracting the photon counts**

The free parameters in the fitting of the asteroid-pointing detectors were the intensities of the fluorescence lines from each major element (Mg, Al, Si, S, Ca, and Fe  $K_\alpha$  and  $K_\beta$ ) entering the top of the instrument, outside the Mg and Al filters; and the gain, zero, and FWHM parameter of the unfiltered detector. The gains, zeroes, and FWHM parameters of the Mg- and Al- filtered detectors were allowed to float within the limits suggested by the calibration-source data (Table 4.12) closest to the date of the flare.

The cosmic-ray background was derived from data taken within 24 hours of the flare while the asteroid was not in the XRS field of view. The “derived parameters” from the processing software included a field-

Table 4.12: XRS Asteroid-Pointing Detector Calibration Data Fitting Results

Date	Gain	Zero	FWHM
Al-filtered			
26-Apr-2000	$0.0386 \pm 0.0002$	$-0.01 \pm 0.04$	$0.385 \pm 0.003$
10-May-2000	$0.0382 \pm 0.0003$	$+0.02 \pm 0.04$	$0.375 \pm 0.004$
24-May-2000	$0.0381 \pm 0.0003$	$+0.02 \pm 0.04$	$0.367 \pm 0.004$
7-Jun-2000	$0.0391 \pm 0.0003$	$-0.09 \pm 0.05$	$0.409 \pm 0.004$
8-Jun-2000	$0.0384 \pm 0.0003$	$+0.03 \pm 0.03$	$0.391 \pm 0.005$
12-Dec-2000	$0.0378 \pm 0.0002$	$+0.03 \pm 0.04$	$0.367 \pm 0.004$
09-Jan-2001	$0.0381 \pm 0.0002$	$-0.05 \pm 0.04$	$0.364 \pm 0.004$
Mg-filtered			
25-Apr-2000	$0.0397 \pm 0.0001$	$+0.02 \pm 0.02$	$0.361 \pm 0.002$
3-May-2000	$0.0397 \pm 0.0002$	$+0.00 \pm 0.03$	$0.358 \pm 0.003$
16-May-2000	$0.0392 \pm 0.0002$	$+0.05 \pm 0.02$	$0.344 \pm 0.002$
23-May-2000	$0.0395 \pm 0.0001$	$+0.01 \pm 0.02$	$0.349 \pm 0.002$
30-May-2000	$0.0407 \pm 0.0003$	$+0.00 \pm 0.01$	$0.428 \pm 0.004$
6-Jun-2000	$0.0399 \pm 0.0002$	$+0.03 \pm 0.03$	$0.378 \pm 0.003$
2-Jan-2001	$0.0402 \pm 0.0002$	$+0.02 \pm 0.02$	$0.373 \pm 0.002$
Unfiltered			
27-Apr-2000	$0.037 \pm 0.002$	$+0.2 \pm 0.3$	$0.33 \pm 0.02$
11-May-2000	$0.035 \pm 0.004$	$+0.4 \pm 0.7$	$0.30 \pm 0.05$
25-May-2000	$0.038 \pm 0.003$	$+0.0 \pm 0.4$	$0.37 \pm 0.04$
20-Dec-2000	$0.037 \pm 0.002$	$+0.3 \pm 0.3$	$0.37 \pm 0.03$

Table 4.13: Unfiltered Detector Characteristics Derived from Flare Data

Date	Gain	Zero	FWHM
4-May-2000	$0.0386 \pm 0.0002$	$-0.06 \pm 0.01$	$0.365 \pm 0.007$
20-May-2000	$0.0378 \pm 0.0008$	$-0.03 \pm 0.03$	$0.366 \pm 0.013$
2-Jun-2000	$0.0395 \pm 0.0020$	$-0.10 \pm 0.11$	$0.430 \pm 0.065$
15-Jun-2000	$0.0387 \pm 0.0006$	$-0.05 \pm 0.03$	$0.371 \pm 0.016$
17-Jun-2000	$0.0384 \pm 0.0007$	$-0.03 \pm 0.03$	$0.380 \pm 0.018$
10-Jul-2000	$0.0375 \pm 0.0007$	$-0.02 \pm 0.03$	$0.350 \pm 0.013$
27-Dec-2000	$0.0389 \pm 0.0003$	$-0.05 \pm 0.01$	$0.375 \pm 0.012$
28-Dec-2000	$0.0391 \pm 0.0006$	$-0.07 \pm 0.03$	$0.351 \pm 0.010$
1-Jan-2001	$0.0387 \pm 0.0005$	$-0.06 \pm 0.02$	$0.354 \pm 0.011$

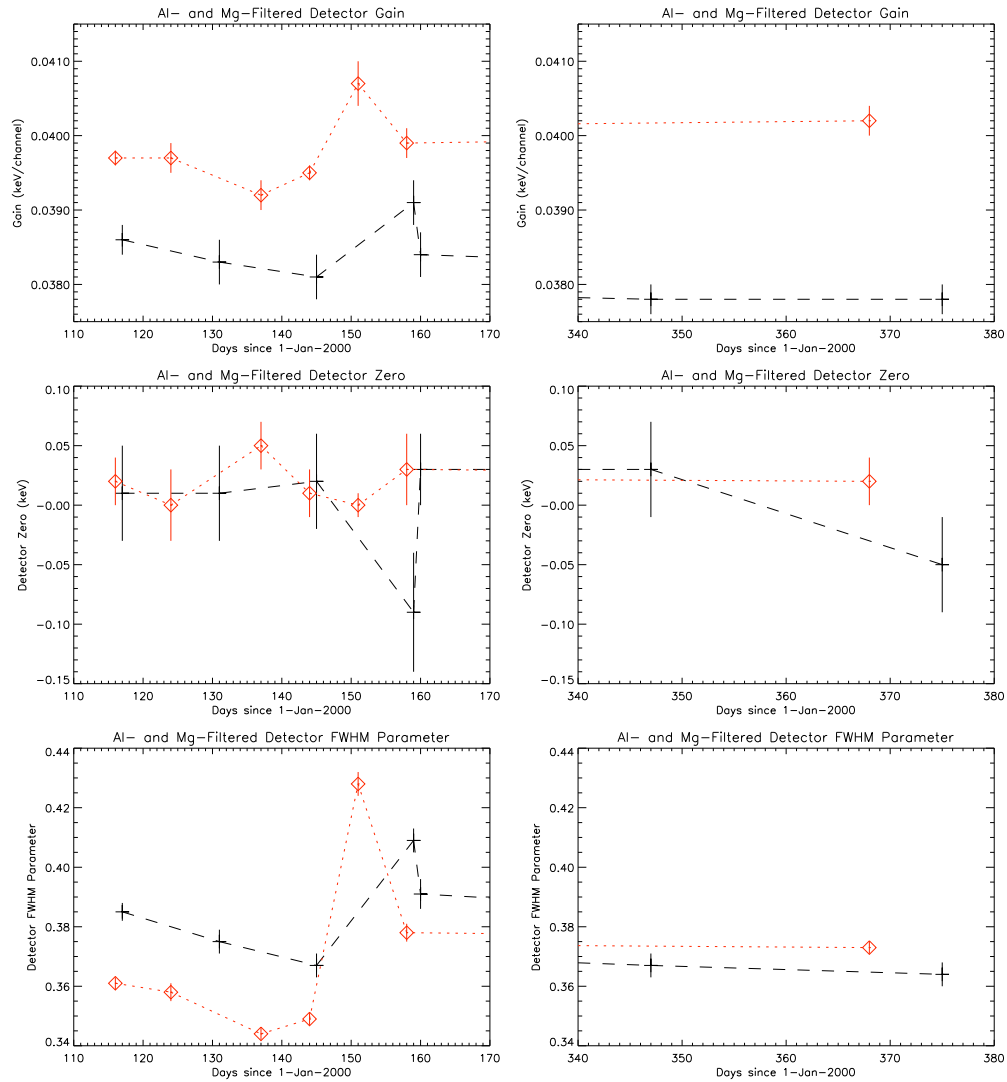


Figure 4.8: Detector properties derived from calibration source data for the Al- and Mg-filtered detectors. The plusses represent the Al-filtered values and the diamonds the Mg-filtered values.

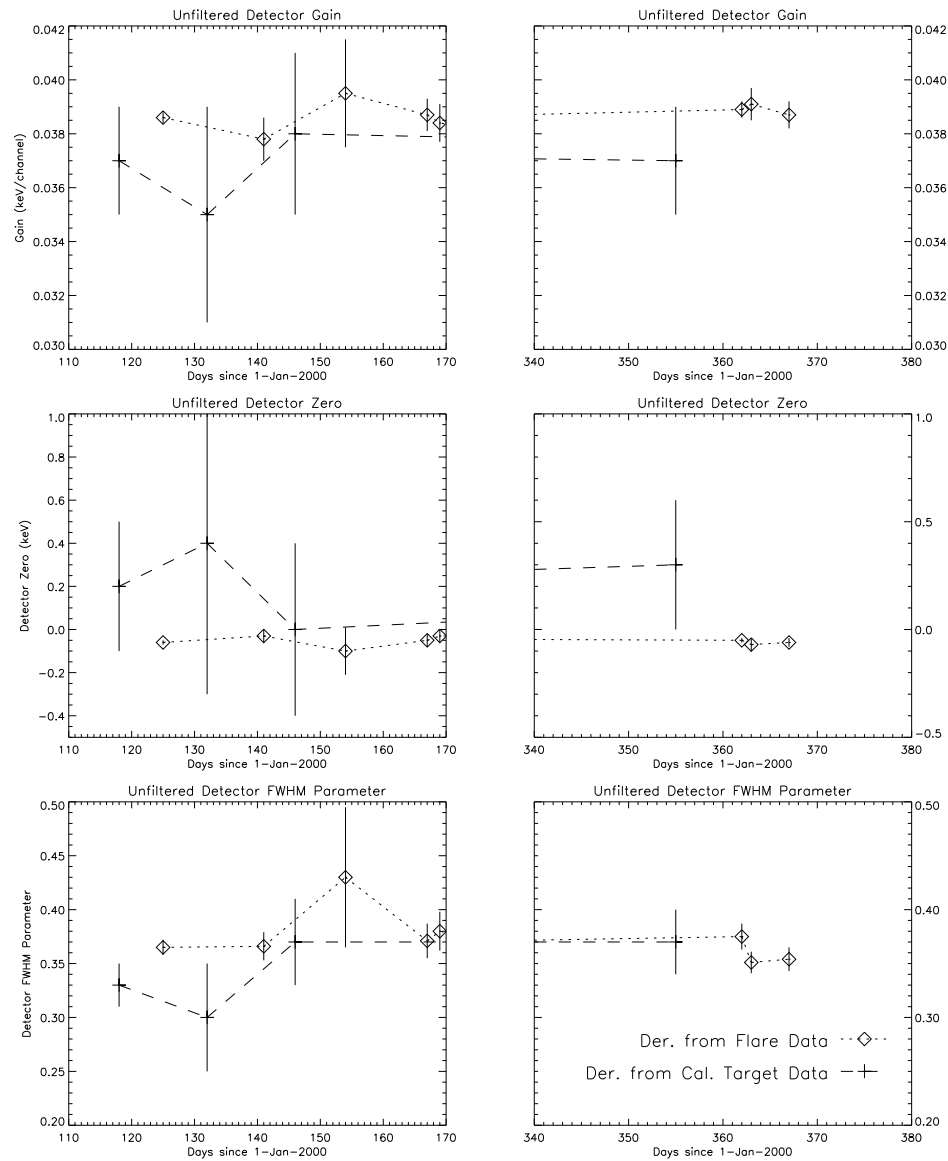


Figure 4.9: Detector properties derived from calibration source data for the unfiltered detector. The plusses mark the cal-target-derived values and the diamonds the flare-derived values.

of-view parameter that sorts the spectra into four categories: FOV=0 was assigned to spectra in which the instrument's  $5^\circ$  field of view contained no asteroid at all; FOV=1 indicated that it was entirely filled with asteroid, and at least part of the field was sunlit; FOV=2 meant that the instrument was seeing entirely dark asteroid; FOV=3 meant that the field of view was partly on the asteroid and partly in space, but at least some of the visible asteroid was lit; and FOV=4 that the instrument was seeing partly dark asteroid and partly space. For the estimate of the cosmic-ray background, spectra with FOV=0, 2, or 4 were added together and scaled to the live time of the relevant flare.

This background was generally constant on time scales of a few hours, as evidenced by the results of the calibration-source fitting, in which the background data had been allowed to float.

The fitting process is illustrated in Figures 4.10 and 4.11. In each of the three plots, the black lines with error bars are the actual data from each asteroid-pointing detector. The orange line is the total fit. The background component is the turquoise line; each of the individual fluorescence lines is represented by a different colored Gaussian.

Table 4.15 lists the resulting photon ratios for five solar flares from May-July 2000, two from December 2000, and one from 2 January 2001.



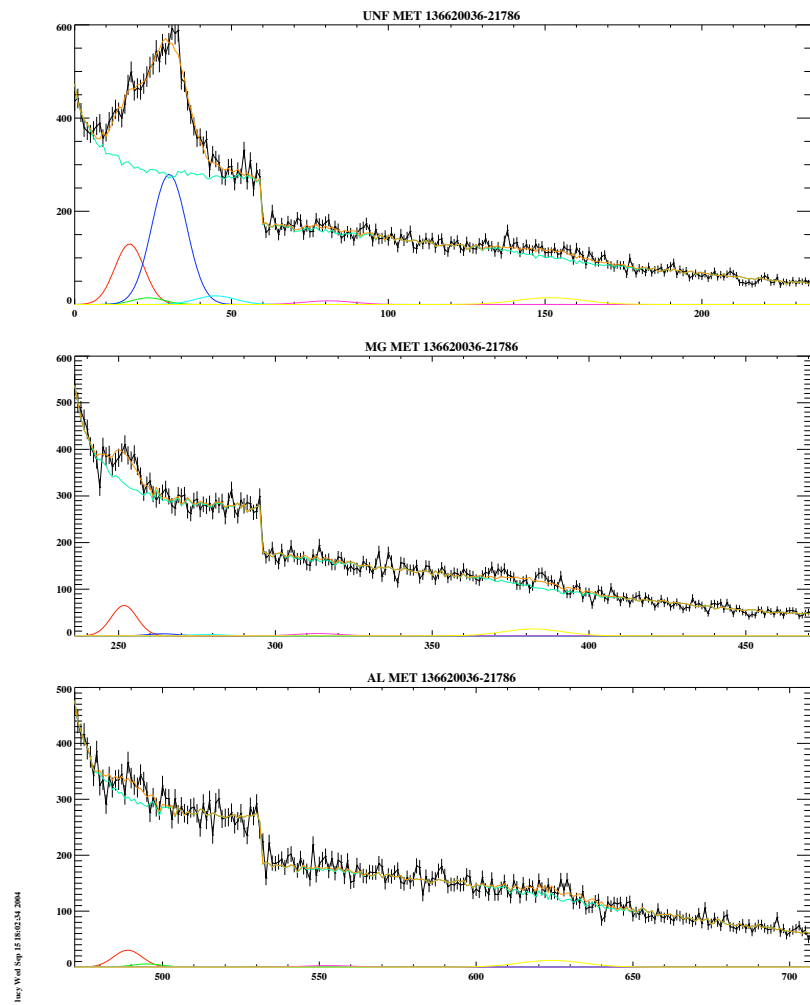


Figure 4.10: Flare Data from 17 June 2000

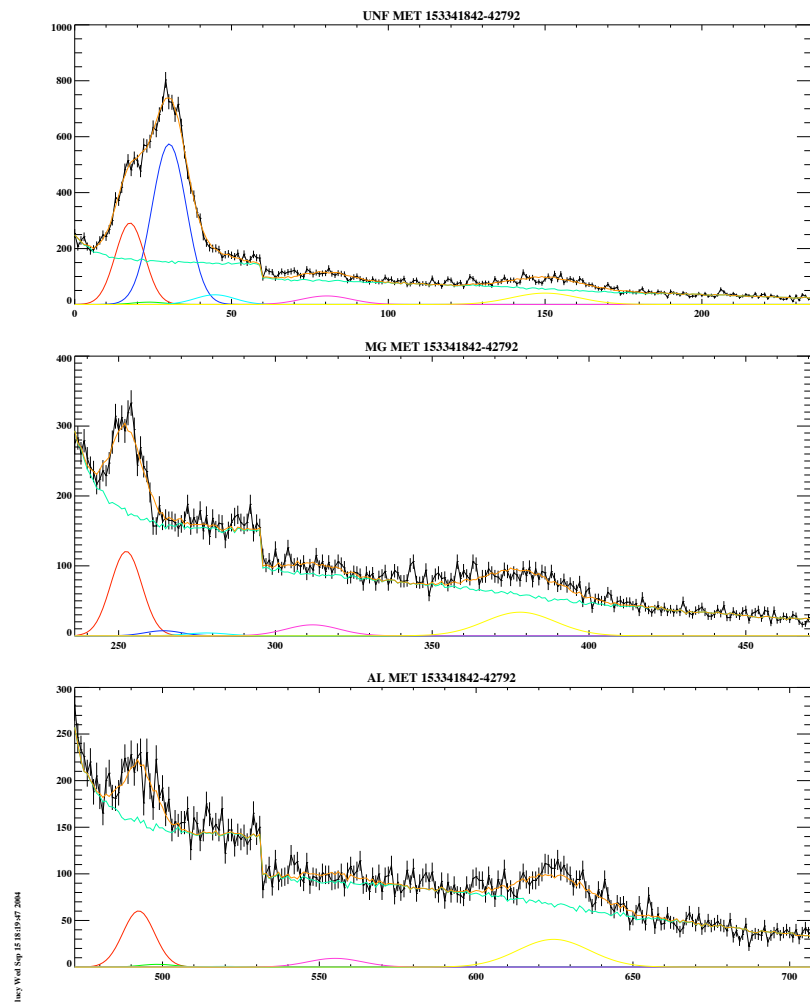


Figure 4.11: Flare Data from 27 December 2000

Table 4.14: Geometric Information for Eight Solar Flares

Date	Flare MET Range	Incidence Angle		Emission Angle		Phase Angle	
		first	last	first	last	first	last
4-May	MET 132826285-27185	35.9°	20.7°	35.2°	58.8°	113.6°	113.7°
20-May	MET 134210436-12886	49.7°	30.5°	49.6°	47.2°	106.3°	104.3°
15-Jun	MET 136508736-10886	32.8°	77.0°	62.4°	47.5°	96.3°	94.9°
17-Jun	MET 136620036-21786	66.6°	43.7°	38.3°	39.6°	92.3°	100.2°
10-Jul	MET 138677136-80836	59.2°	55.4°	48.8°	40.3°	81.1°	87.8°
27-Dec	MET 153341842-42742	68.7°	43.5°	76.1°	42.2°	105.4°	105.5°
28-Dec	MET 153418442-19292	42.7°	85.3°	54.8°	27.4°	84.6°	86.4°
2-Jan	MET 153832142-34142	61.2°	64.2°	31.3°	35.7°	100.4°	101.9°

Date	Flare MET Range	Boresight Lat.		Boresight Long.	
		Range	Mean	Range	Mean
4-May	MET 132826285-27185	+24.2 – +7.9°	+16.8°	+139.4 – +154.8°	+145.8°
20-May	MET 134210436-12886	+33.8 – +38.5°	+36.7°	+151.5 – +154.3°	+154.0°
15-Jun	MET 136508736-10886	+17.7 – -32.4°	-22.1°	+68.5 – -175.5°	+151.7°
17-Jun	MET 136620036-21786	-6.7 – -7.6°	-3.7°	+58.5 – +169.3°	63.8°
10-Jul	MET 138677136-80836	+2.5 – +11.8°	+8.3°	-135.1 – -100.2°	-125.9°
27-Dec	MET 153341842-42742	-3.7 – -7.4°	-4.9°	+163.3 – -174.9°	+174.3°
28-Dec	MET 153418442-19292	-23.8 – -17.8°	-19.9°	-122.0 – -94.6°	-107.8°
2-Jan	MET 153832142-34142	-29.7 – -23.1°	-26.7°	+85.1 – +144.0°	+110.0°

### 4.3 Photon Ratio to Element Ratio Conversion

As described in §3.7, the fluorescence in any line that escapes the asteroid depends not only on the abundance of the fluorescing element, but also on the abundance of all other elements in the asteroid surface that can absorb incident solar radiation on the way in or fluorescent radiation on the way out. Because of this, it was necessary to make some assumptions about the entire composition of the asteroid in order to interpret our data, not just the elements whose fluorescence we could measure. We based our interpretation of the relationships between flu-

Table 4.15: Photon Counts and Ratios for Eight Solar Flares

Flare METs	Photon Counts					
	Mg	Al	Si	S	Ca	Fe
MET 132826285-27185	15614 $\pm$ 451	1360 $\pm$ 469	17249 $\pm$ 362	830 $\pm$ 121	910 $\pm$ 71	1707 $\pm$ 59
MET 134210436-12886	16815 $\pm$ 656	1492 $\pm$ 781	12799 $\pm$ 466	301 $\pm$ 161	56 $\pm$ 92	267 $\pm$ 69
MET 136508736-10886	7386 $\pm$ 472	902 $\pm$ 380	7893 $\pm$ 380	154 $\pm$ 147	399 $\pm$ 90	665 $\pm$ 69
MET 136620036-21786	5795 $\pm$ 401	417 $\pm$ 382	6458 $\pm$ 327	391 $\pm$ 134	205 $\pm$ 76	555 $\pm$ 58
MET 138677136-80836	17216 $\pm$ 762	2460 $\pm$ 754	16026 $\pm$ 531	573 $\pm$ 206	679 $\pm$ 127	443 $\pm$ 95
MET 153341842-42742	11894 $\pm$ 405	303 $\pm$ 369	12440 $\pm$ 319	657 $\pm$ 113	642 $\pm$ 64	1426 $\pm$ 53
MET 153418442-19292	10363 $\pm$ 398	1550 $\pm$ 380	9286 $\pm$ 273	373 $\pm$ 90	244 $\pm$ 54	342 $\pm$ 41
MET 153832142-34142	11917 $\pm$ 476	1628 $\pm$ 476	12776 $\pm$ 385	170 $\pm$ 135	499 $\pm$ 81	876 $\pm$ 63
	Photon Ratios					
	Mg/Si	Al/Si	S/Si	Ca/Si	Fe/Si	
MET 132826285-27185	0.90 $\pm$ 0.03	0.079 $\pm$ 0.030	0.048 $\pm$ 0.007	0.05 $\pm$ 0.004	0.098 $\pm$ 0.004	
MET 134210436-12886	1.31 $\pm$ 0.07	0.117 $\pm$ 0.061	0.023 $\pm$ 0.013	0.004 $\pm$ 0.007	0.021 $\pm$ 0.005	
MET 136508736-10886	0.94 $\pm$ 0.07	0.114 $\pm$ 0.058	0.020 $\pm$ 0.019	0.051 $\pm$ 0.012	0.084 $\pm$ 0.010	
MET 136620036-21786	0.90 $\pm$ 0.08	0.065 $\pm$ 0.059	0.061 $\pm$ 0.021	0.032 $\pm$ 0.012	0.086 $\pm$ 0.010	
MET 138677136-80836	1.11 $\pm$ 0.06	0.078 $\pm$ 0.031	0.031 $\pm$ 0.012	0.036 $\pm$ 0.007	0.028 $\pm$ 0.005	
MET 153341842-42742	0.96 $\pm$ 0.04	0.024 $\pm$ 0.030	0.053 $\pm$ 0.009	0.052 $\pm$ 0.005	0.115 $\pm$ 0.005	
MET 153418442-19292	1.12 $\pm$ 0.05	0.167 $\pm$ 0.041	0.040 $\pm$ 0.010	0.026 $\pm$ 0.006	0.037 $\pm$ 0.005	
MET 153832142-34142	0.93 $\pm$ 0.05	0.127 $\pm$ 0.037	0.013 $\pm$ 0.011	0.039 $\pm$ 0.006	0.069 $\pm$ 0.005	

orescence ratios and elemental ratios on data from meteorites.

Once the incident solar spectrum was modelled, the X-ray fluorescence spectra as would have been induced by the model solar spectrum at the applicable incidence, emission, and phase angles were calculated for a sample of meteorites of different classes (Table 4.16). This is the same method described and used by Nittler et al. (2001). Calibration curves were derived by plotting actual meteorite elemental abundance ratios against calculated meteorite fluorescence ratios and fitting quadratic curves to these points, which would be the formula for converting fluorescent-photon ratios to elemental ratios for that particular incident solar spectrum and geometry. Figure 4.12 illustrates the calibration curves for the solar spectrum and geometry of the major flare from 17 June 2000.

The coherent scattering background (§3.7.2) has been accounted for by inclusion in these calculated meteorite fluorescence ratios, rather than by any attempt to subtract it from the fluorescent photon signal. The induced Al fluorescence in the Al filter has been treated similarly. For this reason, the photon ratios for Al/Si and S/Si in the calibration curves (Figure 4.12) are nonzero even at zero concentrations of Al and S — although there is no actual fluorescence originating from the asteroid, there is still background that will be indistinguishable from fluorescence in the detectors.

The angles came from the spatial derived parameters of the processing software. The phase angles were exact, but the incidence and emis-

Table 4.16: Meteorite Samples Used to Convert Photon Ratios to Element Ratios

Sample	Meteorite	Ref. Num.	Type	Class	Method
d16	ALH77081	N-12	whole-rock	Acapulcoite	wet?
g7	Bustee	W-20	whole-rock	Aubrite	mp-modal
s199	Brachina	J-05	whole-rock	Brachinite	wet
s23	Bali	J-05	whole-rock	CV3	wet
j38	A881526	Y-02	whole-rock	Diogenite	wet
j85	Y793164	Y-02	whole-rock	Monomict Eucrite	wet
d1620	Brient	D-03	whole-rock	Polymict Eucrite	wet
j68	Y790113	Y-02	whole-rock	Polymict Eucrite	wet
s38	Avanhandava	J-05	whole-rock	H4	wet
s61	Ipiranga	J-05	whole-rock	H5	wet
s69	Pulsora	J-05	whole-rock	H5	wet
s239	El Taco	J-05	Sil. Incl. 3	IAB	wet
s176	Semarkona	J-05	whole-rock	LL3	wet
s178	Greenwell Spr.	J-05	whole-rock	LL4	wet
s181	Cherokee Spr.	J-05	whole-rock	LL6	wet
j505	Y74357	Y-02	whole-rock	Lodranite	wet
j507	Y791493	Y-02	whole-rock	Lodranite	wet
p15	Ilimaes	B-20	whole-rock	Pallasite	var
j525	Jalanash	Y-02	whole-rock	Ureilite	wet
j516	Y074659	Y-02	whole-rock	Ureilite	wet
s225	ALH77257	J-05	whole-rock	Ureilite	wet
s176	Semarkona	J-05	whole-rock	LL3 <sup>a</sup>	wet

---

References:

N-12 = Nagahara & Ozawa, 1986, NIPR MEM Spec Is 41:181

W-20 = Watters and Prinz, 1979, "Aubrites - Their origin and relationship to enstatite chondrites," Proc. Lunar. Planetary Sci. 10, 1073-1093.

J-05 = Jarosewich, 1990, Meteoritics 25:323

Y-02 = Yanai & Kojima, 1995, Catalog of the Antarctic Meteorites (book)

D-03 = Dyakonova & Kharitonova, 1961 21:52, Meteoritika (Russian)

B-20 = Buseck, 1977, Geochim. Cosmochim. Acta 41:711

---

<sup>a</sup>Used by Nittler et al. (2001) as the basis for an "LL3 without sulfur" composition. The sulfur abundance was set to zero and all other elements normalized to 100%.

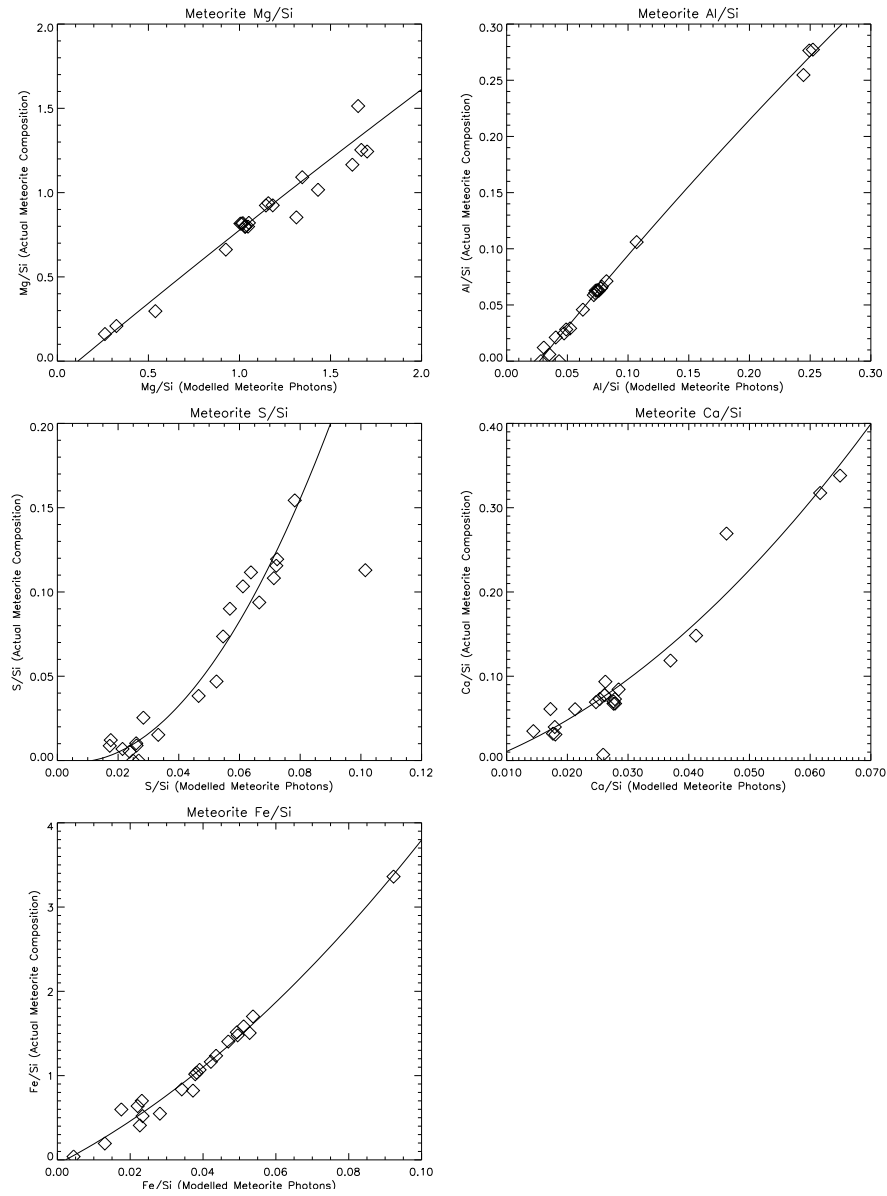


Figure 4.12: Theoretical calibration curves for meteoritic material illuminated by a flare from 17 June 2000. Geometry:  $\theta_{inc} = 59.3^\circ$ ,  $\theta_{emiss} = 42.4^\circ$ ,  $\theta_{phase} = 97.6^\circ$

sion angles were averages over all the “plates” of the NLR-derived shape model that were illuminated and within the XRS field of view at the time. Clearly, however, the incidence and emission angles that matter physically for X-ray interactions are on a much smaller scale than any possible shape model of the asteroid. This is a known limitation of our analysis.

A further correction had to be made because the elements are not spread uniformly throughout the asteroid material, but tend to be grouped together in minerals on spatial scales that are important to X-ray absorption and scattering. Nittler et al. (2001) therefore computed synthetic spectra for major minerals found in non-carbonaceous meteorites (olivine, pyroxene, feldspar, Fe-Ni metal and iron sulfide) as illuminated by solar X-rays at a range of temperatures. These spectra were then combined according to the volume fractions of each mineral in various meteorites to produce synthetic meteorite spectra. The ratios of fluorescence lines in these spectra were compared to those derived from homogeneous models of the same composition. The resulting mineral-mixing correction factors are Table 2 in Nittler et al. (2001), reprinted here as Table 4.17.



Table 4.17: Effect of mineral mixing vs. homogeneous compositions for predicted x-ray fluorescence ratios. After Nittler et al. (2001)

Ratio	Homogeneous Model/Mixing Model				
	R Chond.	LL Chond.	H Chond.	Eucrite	Chondrite Average
Mg/Si	1.11	1.05	0.95	1.23	$1.04 \pm 0.08$
Al/Si	0.70	0.76	0.80	0.81	$0.76 \pm 0.05$
S/Si	1.28	1.29	1.45	1.08	$1.34 \pm 0.10$
Ca/Si	1.05	1.08	1.25	0.95	$1.12 \pm 0.10$
Fe/Si	1.18	1.29	1.78	1.20	$1.42 \pm 0.32$

## 4.4 Specific Solar Flares

### 4.4.1 4 May 2000

The May 4, 2000 solar flare induced more asteroid fluorescence from the high-Z elements (Fe, Ca, and S) than any other solar flare measured by NEAR. The measurements of the Fe/Si, Ca/Si, and S/Si fluorescent photon ratios, therefore, are subject to lower statistical uncertainties than for any other flare. However, because of the high off-normal angle of the gas solar monitor with respect to the Sun ( $\theta_{mean} = 35.5^\circ$ ), the derivation of the solar spectrum for this flare (and therefore the interpretation of the photon ratios from this flare in terms of elemental abundances) is also the most sensitive to the graded filter dimensions.

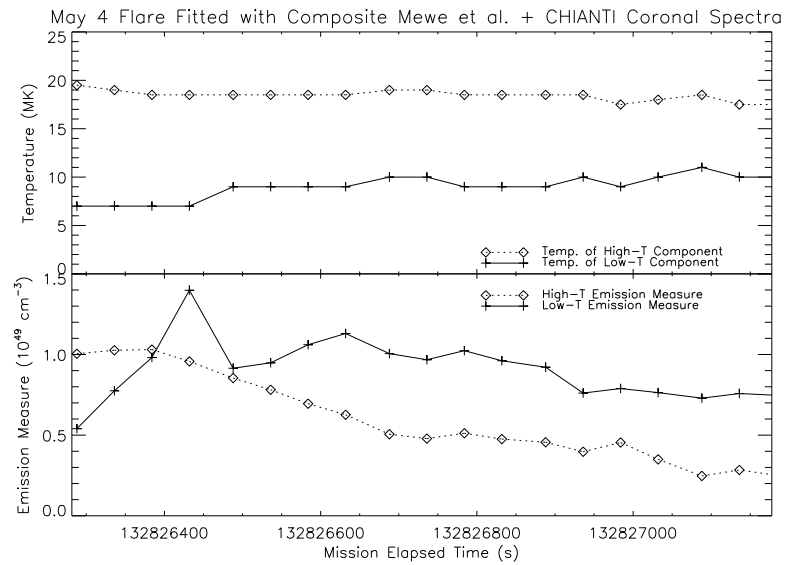
This sensitivity is illustrated in Figure 4.13. The top plot illustrates the temperatures and emission measures of the two-component fit over time for a graded filter model with a Delrin layer 8% thinner than specified. The bottom plot also shows temperatures and emission mea-

tures, but for a graded filter with nominal Delrin thickness. Because the low-energy solar flux is almost entirely cut off from the pinhole in the thicker-Delrin model, the emission measure of the low-T component must be several times higher in order to account for the measured low-T flux than in the thin-Delrin model.

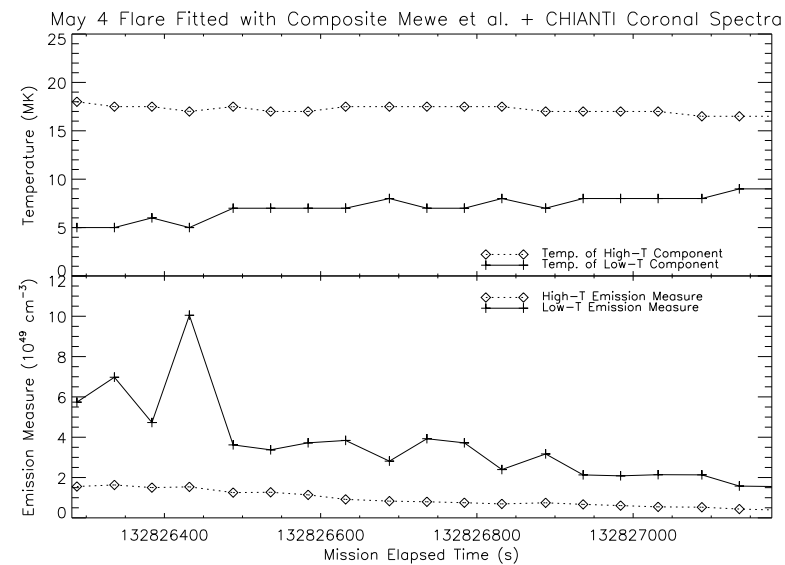
In the asteroid-pointing detectors, the Al photon count and Al/Si photon ratio were very sensitive to any limits placed on the zero point of the Al-filtered detector. In this case, the calibration-source data from April 26 and May 10 (Table 4.12) suggest that the Al detector zero should be above -0.04. When so limited, the Al/Si photon ratio is  $0.092 \pm 0.032$ . However, if the Al-filtered detector zero is allowed to float without a limit, its value drops to -0.09 and the Al/Si photon ratio to  $0.066 \pm 0.024$ . The discrepancy between these solutions has been treated as a systematic uncertainty and included in the total uncertainty quoted in Table 4.15. The effects on the other element ratios were minor compared to the uncertainties from counting statistics.

#### **4.4.2 20 May 2000**

The high-temperature component of this flare was weak relative to the low-temperature component. This “softer” X-ray spectrum induced few iron counts in the asteroid. A favorable spacecraft geometry with respect to the asteroid, however, enabled significant Mg, Al, and Si fluorescence to be measured by the asteroid-pointing detectors.



(a) Composite Spectra: Delrin thickness 92%, Delrin pinhole 105%



(b) Composite Spectra: Delrin thickness 100%, Delrin pinhole 105%

Figure 4.13: Temperatures and emission measures vs. time for the May 4, 2000 solar flare. Top: Composite solar model with a “thin-Delrin” model of the graded filter. Bottom: The same composite solar models, but with a thicker-Delrin graded filter.

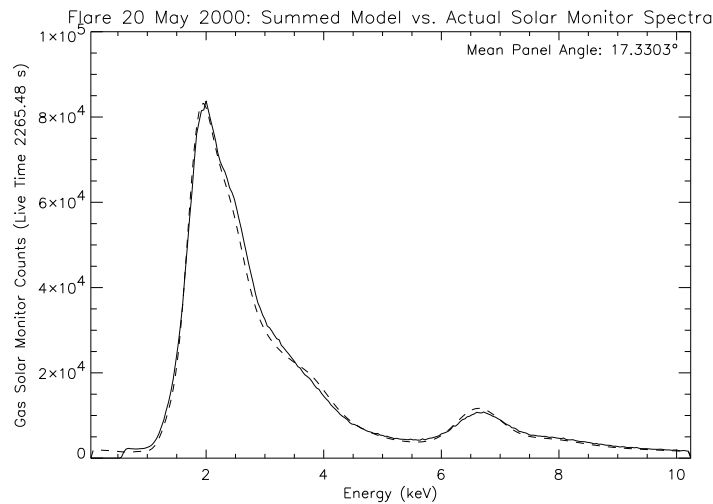
Although the weighted-mean high-temperature component in Figure 4.14 is lower for the CHIANTI fit than for the composite model, the CHIANTI-only number is dominated by five integrations toward the end of the flare in which the “high temperature” component had a relatively low temperature but a high emission measure. In reality, the high-T component in the CHIANTI-only fit is hotter than that in the composite fit during most of the flare (Figure 4.15).

As with the May 4 flare and several other flares, a systematic uncertainty in the Al/Si photon ratio due to uncertainty in the Al-filtered detector zero is included in Table 4.15.

### **4.4.3 15 June 2000**

Model spectra from this event are plotted as Figure 4.16.

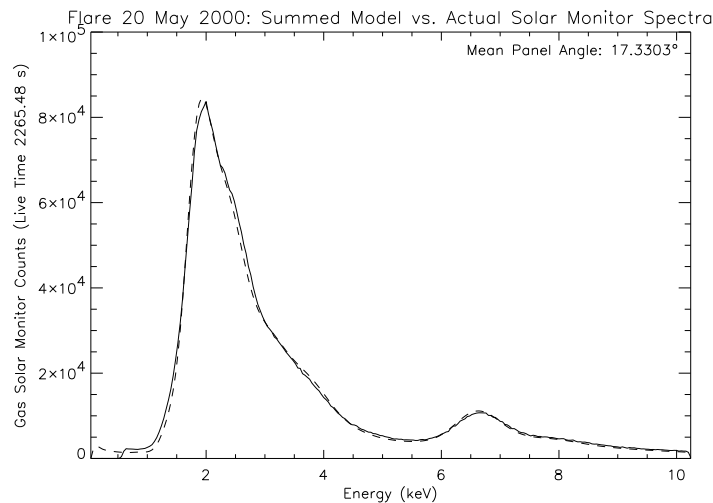
The last calibration-source data between June and August were taken on 8 June 2000, so the calibration-based detector characteristics for the 15 June, 17 June, and 10 July flares are increasingly uncertain. Based on the on the unfiltered detector solutions for these flares (Table 4.13) it would appear that no resolution-degrading event affected the asteroid-pointing detectors during this time period. Upper limits of 0.381 and 0.396 were assigned to the FWHM (resolution) parameters of the Mg- and Al-filtered detectors based on the 6–8 June calibration data.



(a) New CHIANTI Theoretical Spectra:

Mean High-Temperature Component: 14.2 MK ( $EM=0.03 \cdot 10^{49} \text{ cm}^{-3}$ )

Mean Low-Temperature Component: 9.8 MK ( $EM=0.60 \cdot 10^{49} \text{ cm}^{-3}$ )

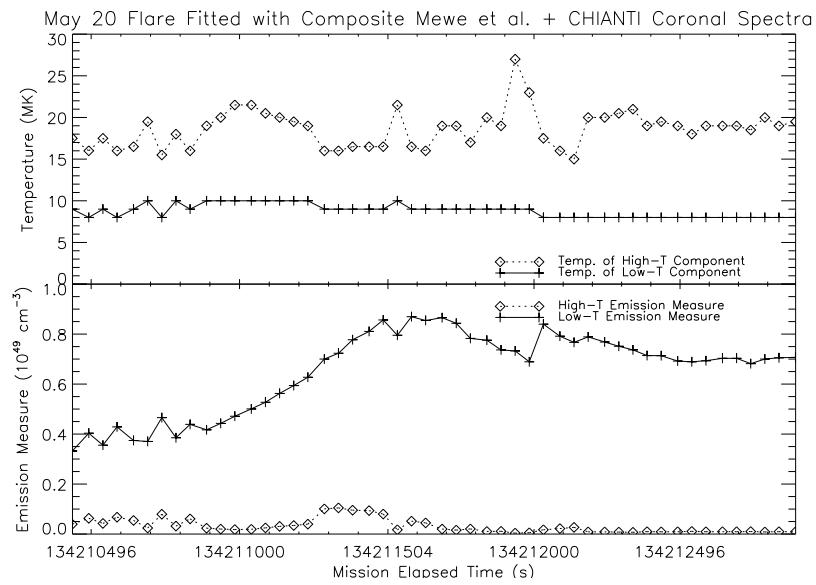


(b) Composite Mewe + CHIANTI Spectra with Ar/Si at the upper limit of Meyer (1985):

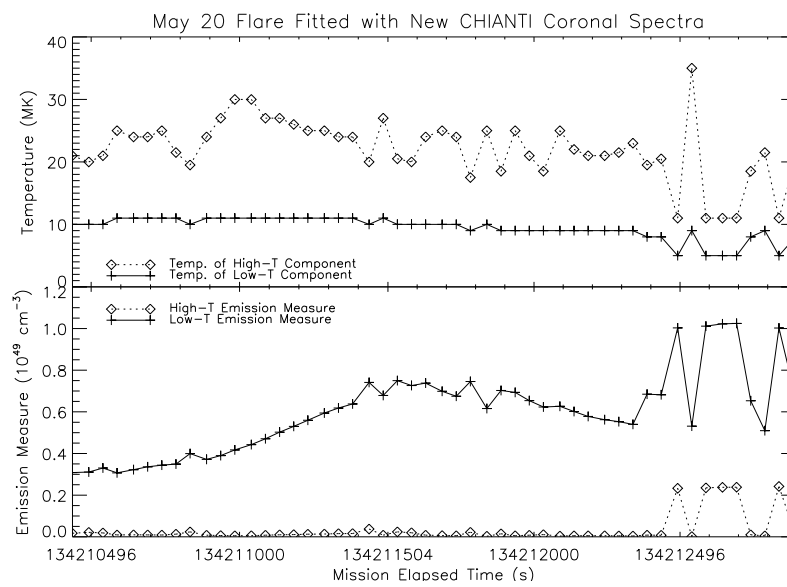
Mean High-Temperature Component: 17.3 MK ( $EM=0.03 \cdot 10^{49} \text{ cm}^{-3}$ )

Mean Low-Temperature Component: 9.2 MK ( $EM=0.65 \cdot 10^{49} \text{ cm}^{-3}$ )

Figure 4.14: May 20 Flare: Actual and Modelled Solar Monitor Output. Solid lines are the sum of 50 gas solar monitor spectra; dashed lines are the sum of the 50 two-temperature models using as input either CHIANTI theoretical solar spectra (top) or the “composite model” (bottom).



(a) Composite Spectra



(b) New CHIANTI Spectra

Figure 4.15: Temperatures and emission measures vs. time for the May 20, 2000 solar flare.

As with the previous flares, the systematic uncertainty in the Al/Si photon ratio due to Al-filtered zero calibration has been included in Table 4.15. The high (limited Al-detector zero) and low (floating zero point) values for Al/Si are  $0.096 \pm 0.058$  and  $0.054 \pm 0.064$  respectively.

#### **4.4.4 17 June 2000**

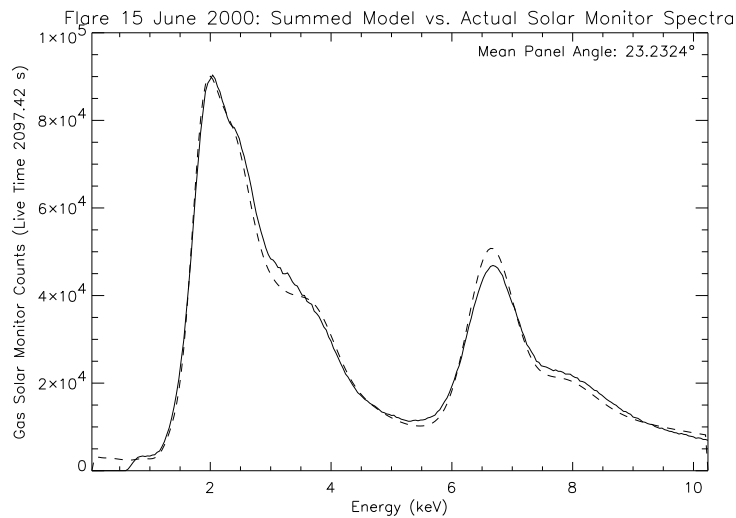
This is the flare represented in Tables 4.10 and 4.11. The temperatures, emission measures, and GOES ratios for this flare are also plotted as Figure 4.18.

This flare was very similar in solar temperature and geometry to the previous flare (15 June). The high- and low- Al/Si solutions are  $0.046 \pm 0.060$  and  $0.022 \pm 0.065$  respectively.

#### **4.4.5 10 July 2000**

Although the panel angle for this flare was the lowest for any major flare, the  $\chi^2$  values of the solar spectral fitting remain high regardless of the graded filter characteristics. The  $\chi^2$  decreases with degraded gas solar monitor resolution (Figure 4.19). Fortunately, the effect of degraded solar monitor resolution on the geochemical results is much less than the uncertainty due to the statistical errors in the photon counts.

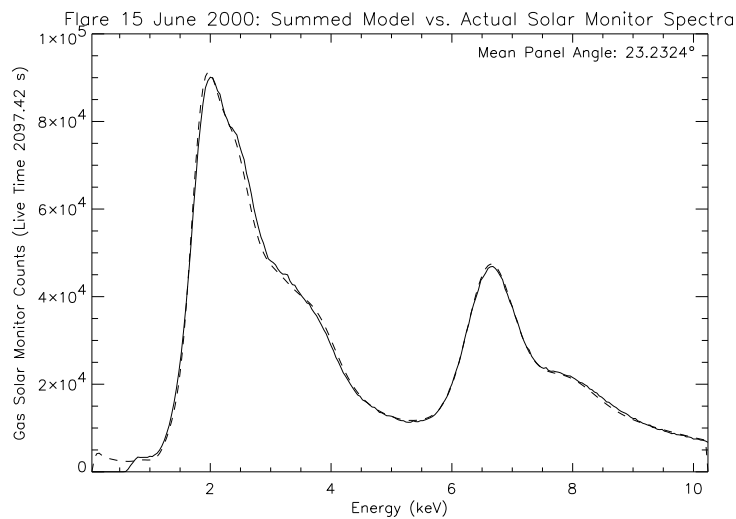
Since no calibration data had been taken for over a month at the time of this flare, no limits on the zero points of the detectors were applied. The



(a) New CHIANTI Theoretical Spectra.

Mean High-Temperature Component: MK ( $EM = 10^{49} \text{ cm}^{-3}$ )

Mean Low-Temperature Component: MK ( $EM = 10^{49} \text{ cm}^{-3}$ )



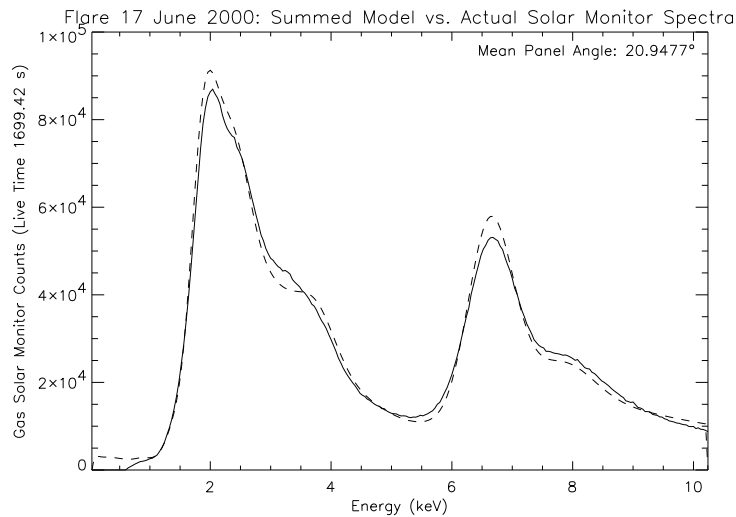
(b) Composite Mewe + CHIANTI Spectra with Ar/Si at the upper limit of Meyer (1985).

Mean High-Temperature Component: MK ( $EM = 10^{49} \text{ cm}^{-3}$ )

Mean Low-Temperature Component: MK ( $EM = 10^{49} \text{ cm}^{-3}$ )

Figure 4.16: June 15 Flare: Actual and Modelled Solar Monitor Output. Solid lines are the sum of gas solar monitor spectra; dashed lines are the sum of the two-temperature models using as input either CHIANTI theoretical solar spectra (top) or the “composite model” (bottom).

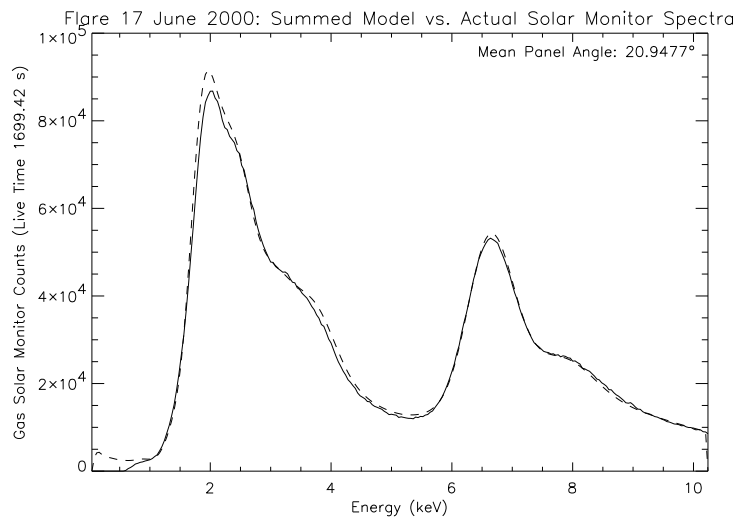




(a) New CHIANTI Theoretical Spectra:

Mean High-Temperature Component: 23.8 MK ( $EM=0.10 \cdot 10^{49} \text{ cm}^{-3}$ )

Mean Low-Temperature Component: 11.8 MK ( $EM=1.05 \cdot 10^{49} \text{ cm}^{-3}$ )

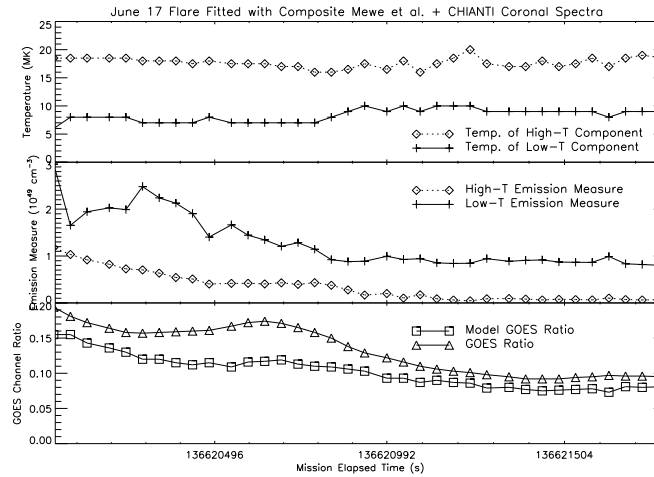


(b) Composite Mewe + CHIANTI Spectra with Ar/Si at the upper limit of Meyer (1985):

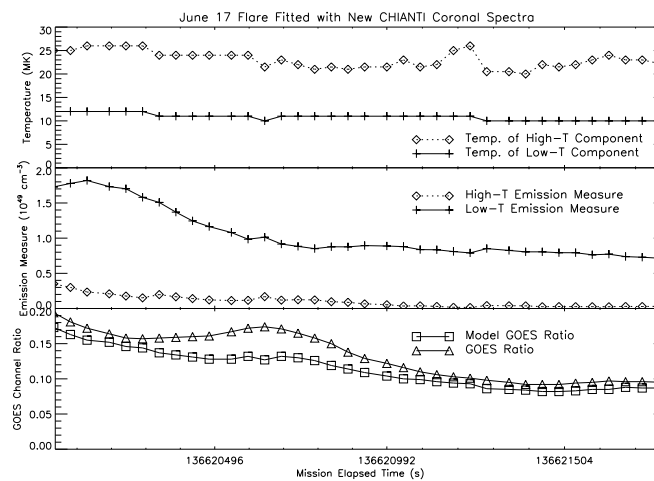
Mean High-Temperature Component: 17.8 MK ( $EM=0.34 \cdot 10^{49} \text{ cm}^{-3}$ )

Mean Low-Temperature Component: 10.0 MK ( $EM=1.29 \cdot 10^{49} \text{ cm}^{-3}$ )

Figure 4.17: June 17 Flare: Actual and Modelled Solar Monitor Output. Solid lines are the sum of 36 gas solar monitor spectra; dashed lines are the sum of the 36 two-temperature models using as input either CHIANTI theoretical solar spectra (top) or the “composite model” (bottom).



(a) Composite Spectra



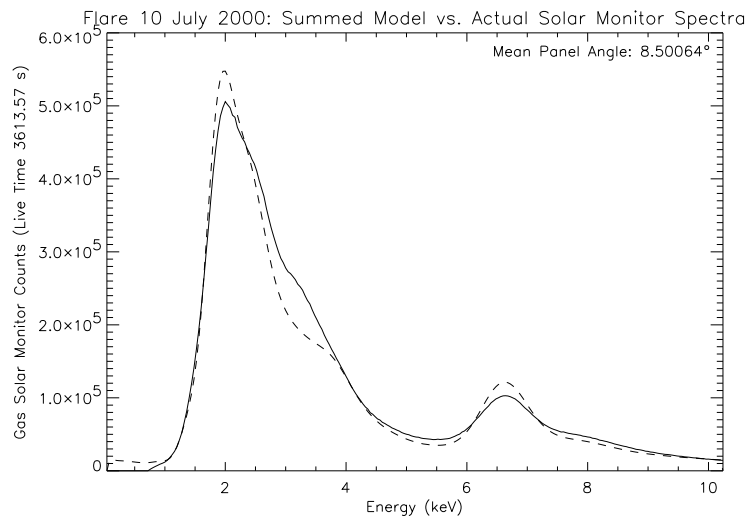
(b) New CHIANTI Spectra

Figure 4.18: Temperatures, Emission Measures, and GOES Ratios vs. time for the June 17, 2000 solar flare. These data are tabulated as Tables 4.10 and 4.11.

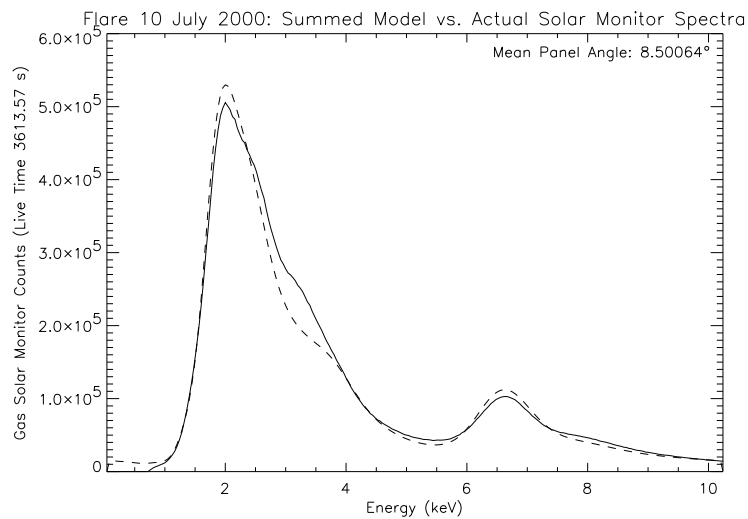
flare-derived resolutions of the asteroid-pointing detectors were 0.360, 0.373, and 0.439 for the unfiltered, Mg-filtered, and Al-filtered detectors respectively. Applying an upper limit of 0.390 to the Al-filtered detector resolution (on the assumption that it usually did not stray too far from the resolution of the unfiltered detector) did not materially change the photon ratios.

#### **4.4.6 27 December 2000**

This flare was unusual in that its solar monitor data were a much better match to the CHIANTI spectra generated with photospheric solar elemental abundances than to either of the coronal-abundance models. The actual and modelled solar monitor data are plotted in Figure 4.20. Because the solar S/Si ratio is four times higher in the photosphere than in the corona, the low-energy “peak” in the gas solar monitor is dominated by the S XV lines around 2.46 keV rather than by the silicon lines just below 2 keV. This distinction is exaggerated by the graded filter, which makes the solar monitor much more sensitive at 2.5 keV than at 1.9 keV. At 11 MK, for example, there is still actually more flux in the 1.9 keV Si XIII line than in the strongest S XV line, even at photospheric solar abundances; and the light-element fluorescence from the asteroid will be excited mainly by Si and Mg XII (1.47 keV) rather than by the S XV photons that show up in the solar monitor.



(a) New CHIANTI Theoretical Spectra, Normal Resolution (FWHM Parameter = 0.340)



(b) Gas Solar Monitor Resolution Degraded by 12%

Figure 4.19: July 10 Flare: Actual and Modelled Solar Monitor Output. Solid lines are the sum of 75 gas solar monitor spectra; dashed lines are the sum of the 75 two-temperature models using as input the new CHIANTI theoretical solar spectra.

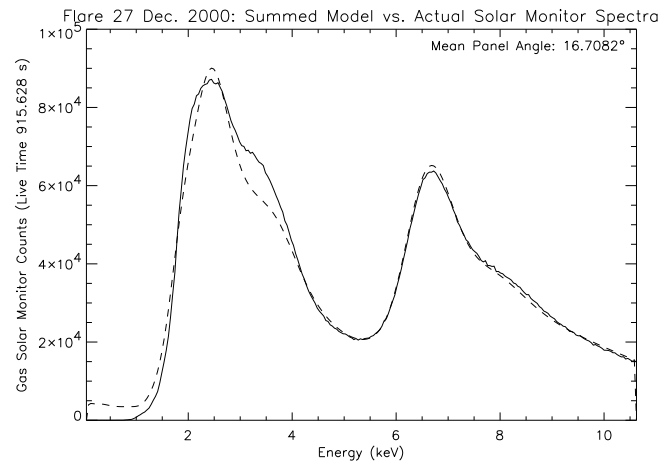


Figure 4.20: Dec. 27 solar flare. The solid line is the sum of 19 gas solar monitor spectra, corrected for zero shift. The low energy channels are undercounted because of this baseline shift effect. The dashed line is the sum of 19 two-temperature “CHIANTI” models with photospheric solar elemental abundances.

The solar monitor gain during this and all subsequent flares was 0.0415 keV/channel, an increase from the 0.040 keV/channel consistently observed during the summer flares. This may have been caused by space charge effects or other types of detector aging. The asteroid-pointing detectors were unaffected, probably because they had counted far fewer X-rays during the course of the mission.

The resolution of the solar detector also appears to have been degraded somewhat during this solar flare. The fit illustrated in Figure 4.20 was done with the resolution degraded by 14%. No corresponding degradation of the asteroid-pointing detectors appears to have taken place (see Table 4.13).

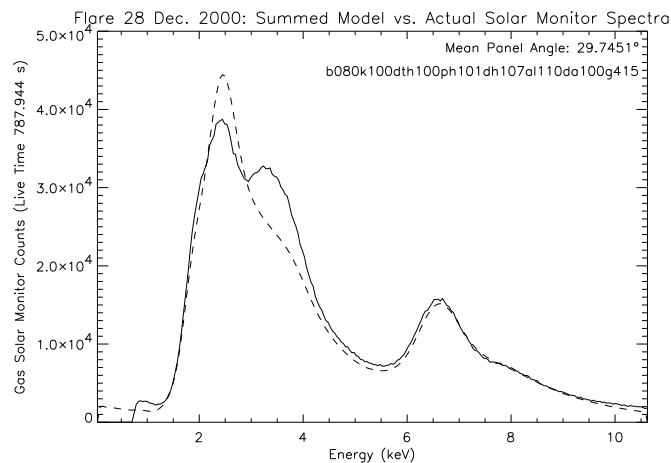


Figure 4.21: Dec. 28 solar flare. The solid line is the sum of 17 gas solar monitor spectra, corrected for zero shift. The low energy channels are undercounted because of this baseline shift effect. The dashed line is the sum of 17 two-temperature “CHIANTI” models with photospheric solar elemental abundances.

#### 4.4.7 28 December 2000

The Dec. 28 flare was not analyzed by Nittler et al. (2001), largely because the solar spectrum could not be modelled satisfactorily at that time. Like the Dec. 27 flare, it is much better modelled with solar photospheric abundances than with coronal abundances. However, the modelling (Figure 4.21) remains less successful in this case, largely because of a very large excess of counts at about 3.5 keV.

Oddly, the high-energy portion of the spectrum, where the detector resolution is most easily observed due to the sparseness of the solar emission lines, is best fit with the detector at optimal resolution. It is difficult to explain how a detector that appeared to have performed at 14% de-

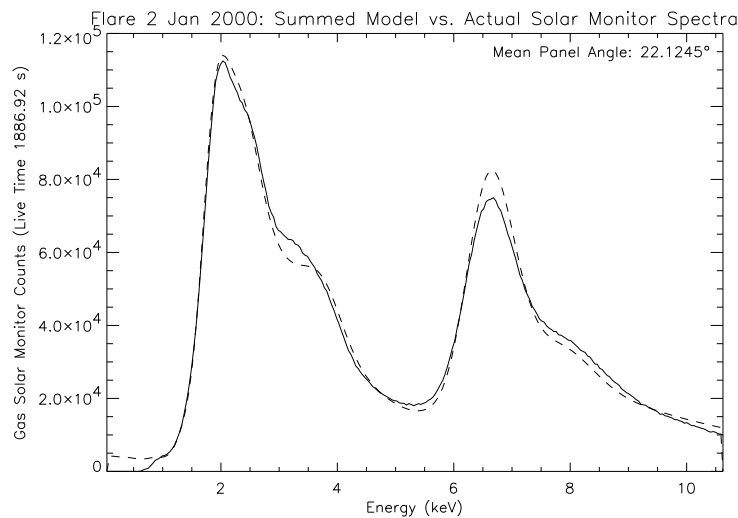
graded resolution less than 24 hours earlier could have recovered so suddenly. Nevertheless, the  $\chi^2$  minimum for the high-energy channels is unmistakably at a higher resolution than it was for the Dec. 27 flare.

The photon ratios for this flare, unlike those for the May 4 flare, are insensitive to restrictions on the asteroid-pointing detector parameters. The Al/Si photon ratio is  $0.17 \pm 0.04$ .

#### **4.4.8 2 January 2001**

Unlike the two preceding flares, this flare is a good match to the coronal-abundance solar spectral models.

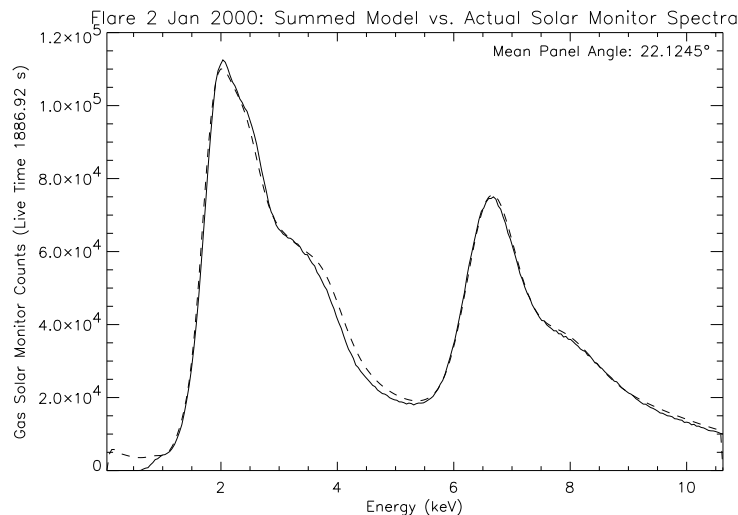
The gain for this flare was 0.0415 keV/channel. The FWHM parameter of the gas solar monitor was increased by 8%. The integrated data from and models of gas solar monitor output are plotted as Figure 4.22.



(a) New CHIANTI Theoretical Spectra:

Mean High-Temperature Component: 20.2 MK ( $EM=0.12 \cdot 10^{49} \text{ cm}^{-3}$ )

Mean Low-Temperature Component: 12.1 MK ( $EM=1.18 \cdot 10^{49} \text{ cm}^{-3}$ )



(b) Composite Mewe + CHIANTI Spectra with Ar/Si at the upper limit of Meyer (1985):

Mean High-Temperature Component: 16.0 MK ( $EM=0.58 \cdot 10^{49} \text{ cm}^{-3}$ )

Mean Low-Temperature Component: 9.8 MK ( $EM=1.27 \cdot 10^{49} \text{ cm}^{-3}$ )

Figure 4.22: Jan. 2 Flare: Actual and Modelled Solar Monitor Output. Solid lines are the sum of 41 gas solar monitor spectra; dashed lines are the sum of the 41 two-temperature models using as input either CHIANTI theoretical solar spectra (top) or the “composite model” (bottom).



## 4.5 Results and Discussion

The elemental ratios calculated using Models 1–7 are tabulated as Tables 4.19–4.25. The elemental ratios derived from all seven models and averaged over all eight solar flares are collected in Table 4.26.

Figure 4.23 illustrates the light-element abundance ratios calculated from the eight solar flares. Figures 4.23 (a–c) show the results from each flare individually when calculated using solar models 1, 4, and 7 respectively. Figure 4.23(d)

Spatial variation?

Space Weathering: Pieters et al. 2000 (?), Hapke Pieters et al. (2000), Hapke (2001)

nanophase iron production

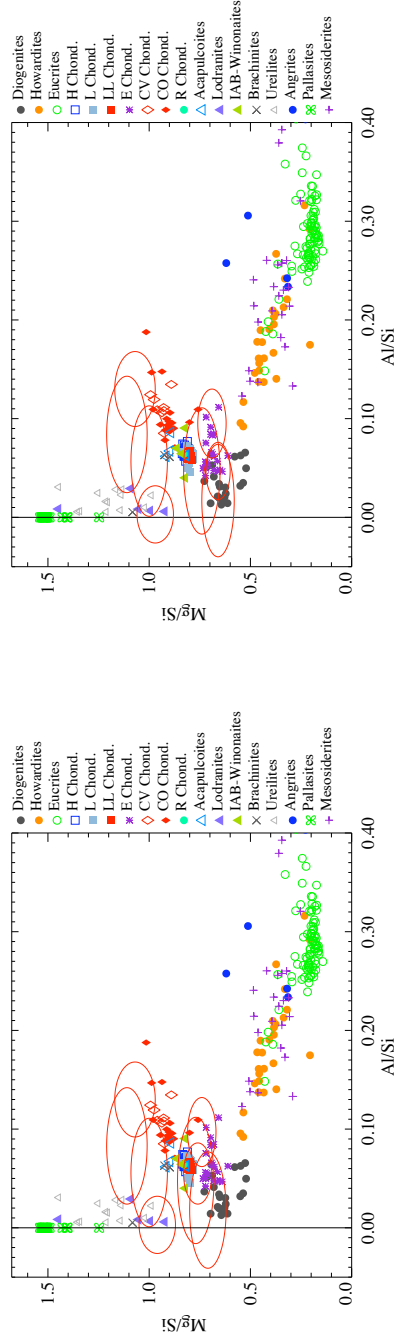
sulfur depletion?

Laser space weathering experiments by Sasaki et al. Sasaki et al. (2001)

Brazil nut effect:

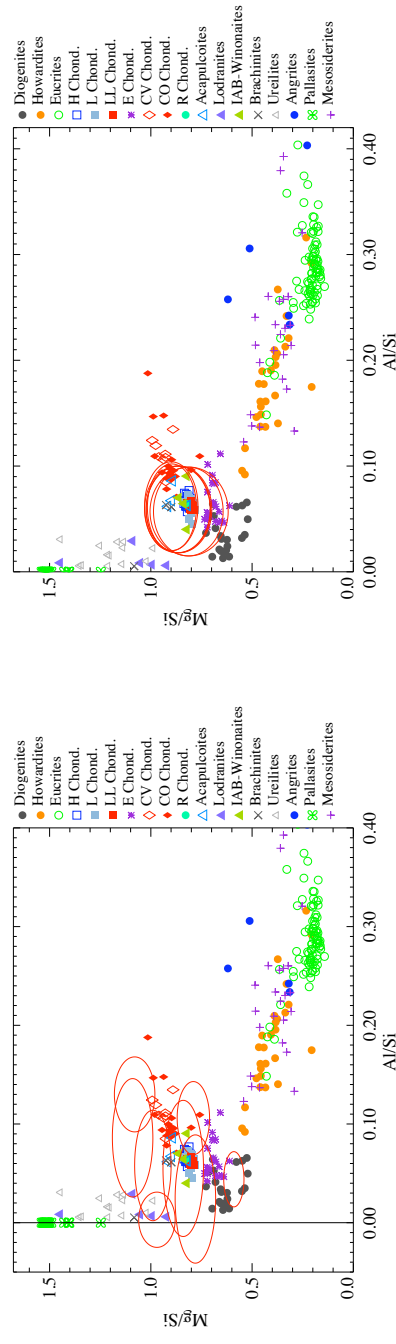
Reverse brazil nut effect:

Gamma ray results: Evans et al. (2001)

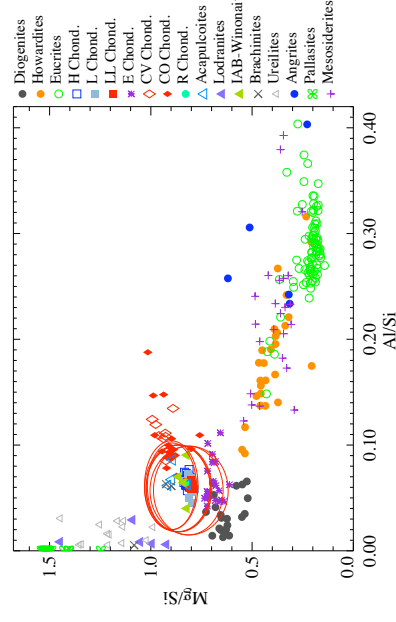


(a) Model 1

(b) Model 4



(c) Model 7



(d) 8-Flare Averages for All Models

Figure 4.23: Mg/Si and Al/Si composition ratios for eight flares analyzed using various solar models. Ellipses represent a combination of  $1-\sigma$  photon statistical uncertainties and uncertainties due to mineral mixing.

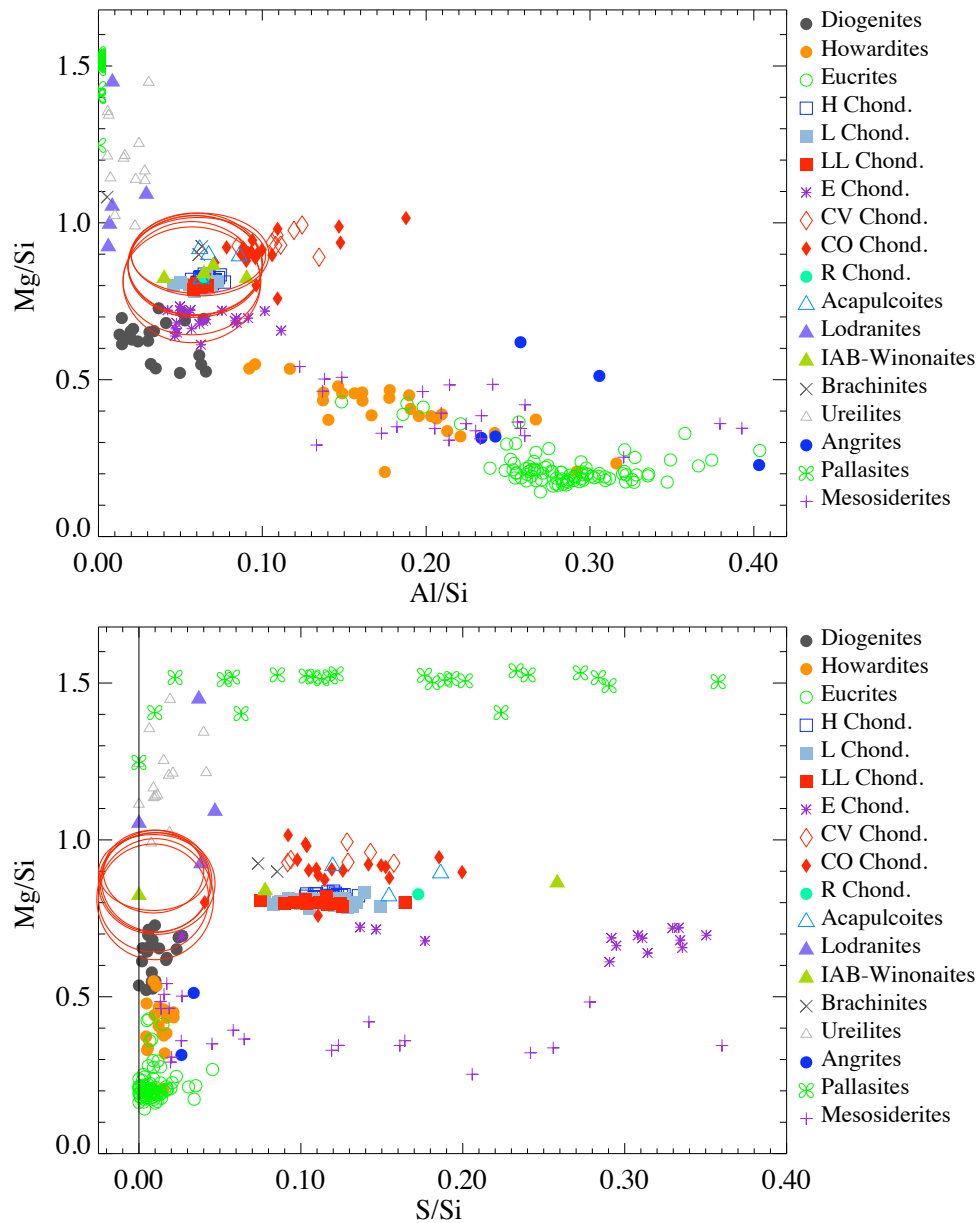


Figure 4.24: Composition results for Models 1-7, averaged over eight solar flares. Models 1-4 use the composite solar spectral model and are arranged in order of increasing Delrin-layer thickness. Models 5 and 6 use the 2004 CHIANTI models only and the graded filter models that give the best GOES-ratio match and  $\chi^2$  value respectively. The black ellipses represent the “Best Eros” values from Nittler et al. (2001).

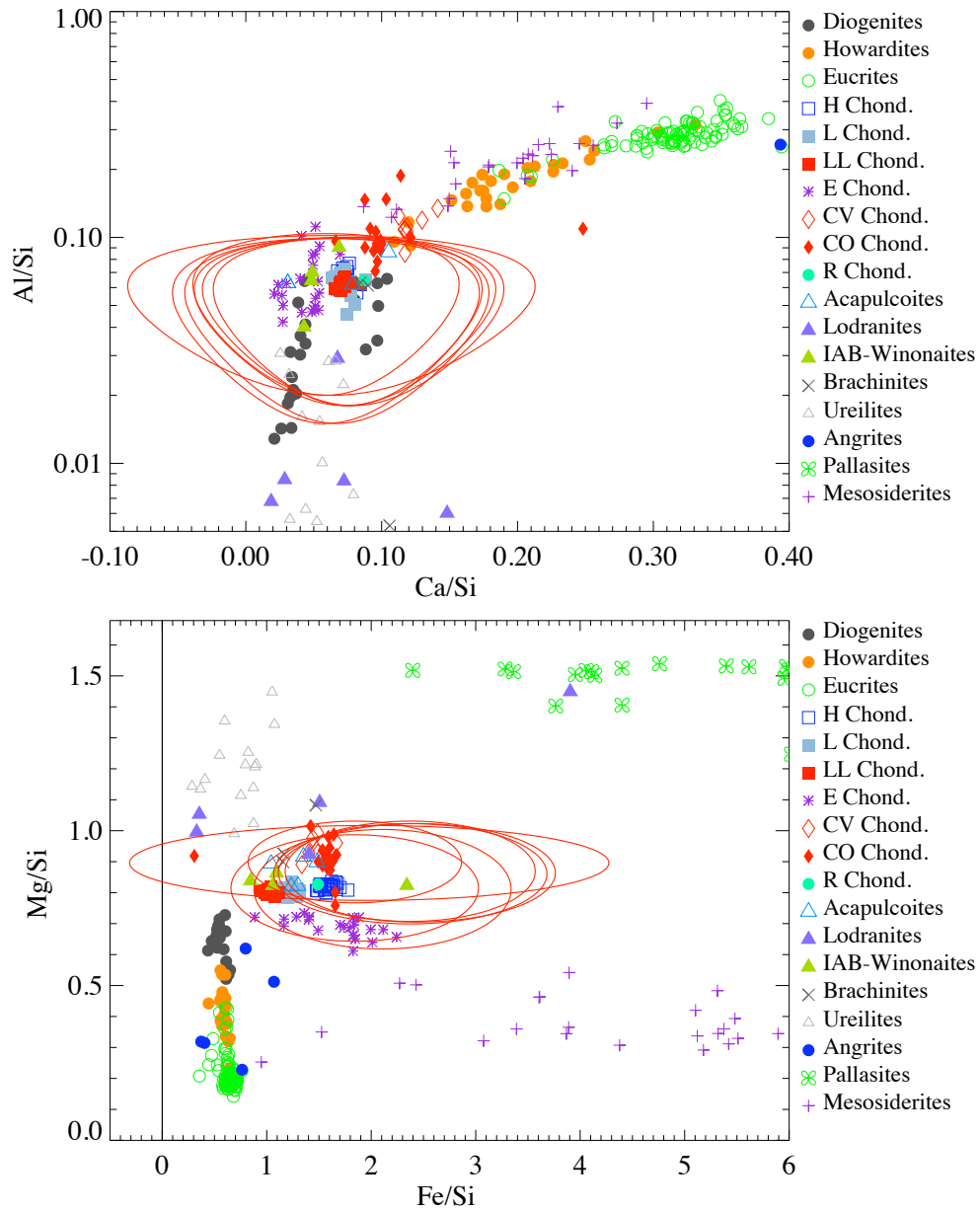


Figure 4.25: Composition results for Models 1-6, averaged over eight solar flares. See Figure 4.24.

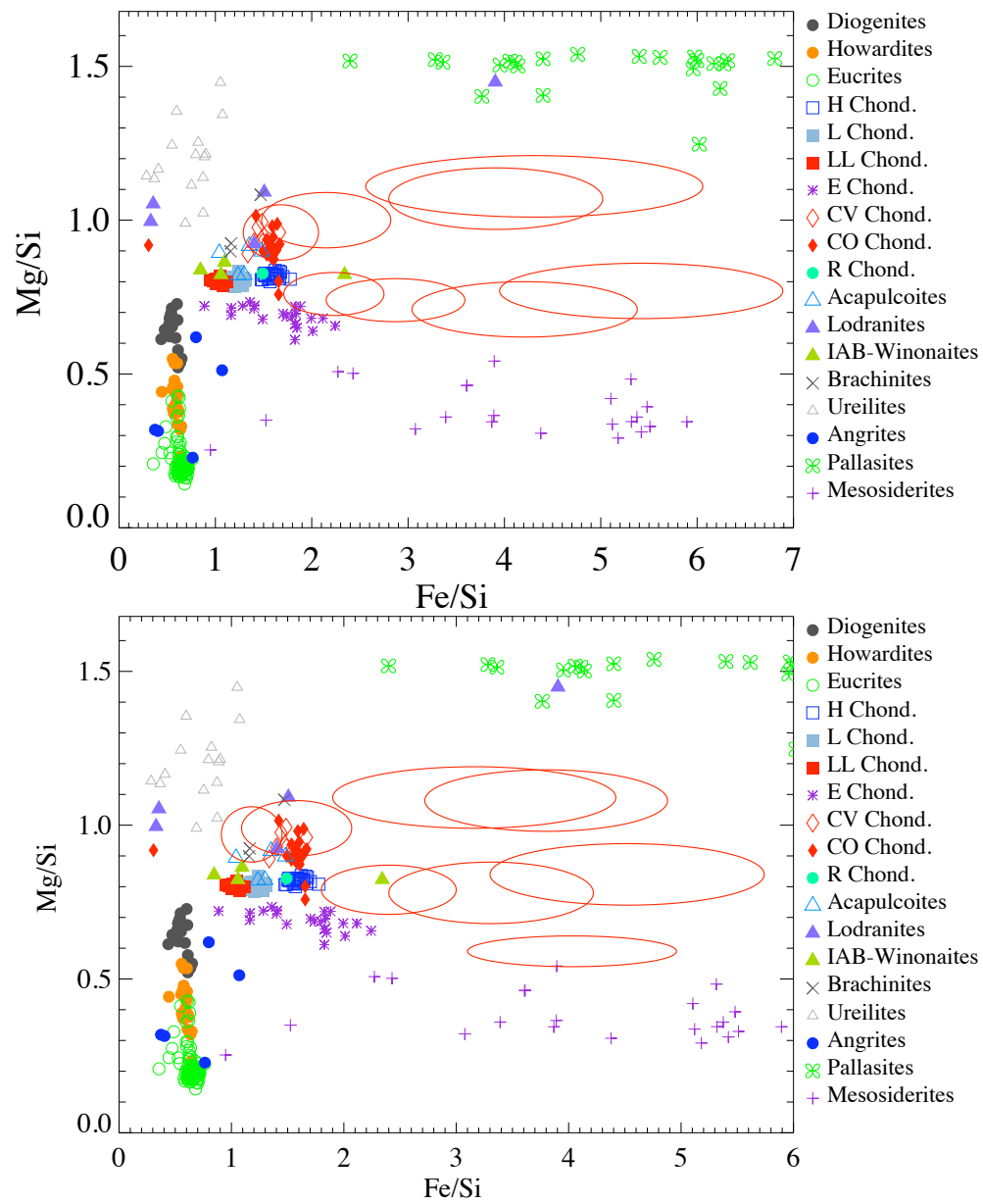


Figure 4.26: Flare-to-flare variations in Fe/Si composition. Top: Model 1. Bottom: Model 7.

Table 4.18: Photon and Element Ratios from Nittler et al. (2001)

## Photon Ratios:

Date	Mg/Si	Al/Si	S/Si	Ca/Si	Fe/Si
2000-May-04	$0.93 \pm 0.03$	$0.08 \pm 0.02$	$0.055 \pm 0.007$	$0.052 \pm 0.004$	$0.101 \pm 0.004$
2000-June-15	$0.96 \pm 0.07$	$0.12 \pm 0.05$	$0.023 \pm 0.017$	$0.047 \pm 0.012$	$0.077 \pm 0.009$
2000-July-10	$1.16 \pm 0.05$	$0.10 \pm 0.04$	$0.009 \pm 0.014$	—	—
2000-Dec-27	$0.97 \pm 0.04$	$0.08 \pm 0.03$	$0.064 \pm 0.008$	$0.054 \pm 0.005$	$0.105 \pm 0.005$
2001-Jan-02	$0.93 \pm 0.04$	$0.14 \pm 0.03$	$0.036 \pm 0.010$	$0.045 \pm 0.007$	$0.080 \pm 0.005$

## Element Ratios (Two-Temperature Fits):

Date	Mg/Si	Al/Si	S/Si	Ca/Si	Fe/Si
2000-May-04	$0.64 \pm 0.02$	$0.04 \pm 0.02$	$0.049 \pm 0.015$	$0.201 \pm 0.026$	$4.32 \pm 0.22$
2000-June-15	$0.70 \pm 0.05$	$0.081 \pm 0.045$	$0.004 \pm 0.011$	$0.152 \pm 0.066$	$3.12 \pm 0.46$
2000-July-10	$0.86 \pm 0.04$	$0.06 \pm 0.03$	$0.0004 \pm 0.0004$	—	
2000-Dec-27	$0.81 \pm 0.03$	$0.05 \pm 0.03$	$0.047 \pm 0.013$	$0.082 \pm 0.012$	$1.32 \pm 0.08$
2001-Jan-02	$0.84 \pm 0.03$	$0.10 \pm 0.03$	$0.011 \pm 0.009$	$0.077 \pm 0.020$	$1.69 \pm 0.12$

## Element Ratios: Single- (High-) Temperature Fits

Date	Mg/Si	Al/Si	S/Si	Ca/Si	Fe/Si
2000-May-04	$0.88 \pm 0.03$	$0.04 \pm 0.02$	$0.026 \pm 0.008$	$0.081 \pm 0.010$	$2.03 \pm 0.10$
2000-June-15	$0.96 \pm 0.06$	$0.083 \pm 0.045$	$0.001 \pm 0.009$	$0.079 \pm 0.034$	$1.75 \pm 0.24$
2000-July-10	$1.16 \pm 0.04$	$0.07 \pm 0.03$	$< 0.0004$	—	
2000-Dec-27	$0.97 \pm 0.04$	$0.05 \pm 0.03$	$0.011 \pm 0.009$	$0.043 \pm 0.007$	$0.75 \pm 0.04$
2001-Jan-02	$0.89 \pm 0.04$	$0.10 \pm 0.03$	$0.010 \pm 0.008$	$0.067 \pm 0.017$	$1.48 \pm 0.11$

Table 4.19: Element Ratios for Eight Solar Flares, Corrected for Mixing Effects: Model 1

	Element Ratios				
	Mg/Si	Al/Si	S/Si	Ca/Si	Fe/Si
MET 132826285-27185	0.76 ± 0.07	0.055 ± 0.031	0.047 ± 0.017	0.17 ± 0.03	2.23 ± 0.52
MET 134210436-12886	1.11 ± 0.10	0.083 ± 0.059	0.018 ± 0.028	0.02 ± 0.02	4.31 ± 1.75
MET 136508736-10886	0.77 ± 0.09	0.048 ± 0.064	0.01 ± 0.02	0.38 ± 0.16	5.42 ± 1.47
MET 136620036-21786	0.71 ± 0.09	0.018 ± 0.059	0.114 ± 0.089	0.12 ± 0.08	4.21 ± 1.17
MET 138677136-80836	1.00 ± 0.09	0.056 ± 0.055	0.022 ± 0.022	0.19 ± 0.07	2.15 ± 0.67
MET 153341842-42742	0.96 ± 0.09	0.003 ± 0.029	0.021 ± 0.010	0.08 ± 0.01	1.68 ± 0.39
MET 153418442-19292	1.07 ± 0.10	0.130 ± 0.038	0.013 ± 0.009	0.06 ± 0.02	3.91 ± 1.11
MET 153832142-34142	0.74 ± 0.07	0.097 ± 0.035	0.000 ± 0.006	0.14 ± 0.04	2.87 ± 0.72
Averages	0.861 ± 0.162	0.059 ± 0.041	0.011 ± 0.036	0.079 ± 0.111	2.374 ± 1.308

Table 4.20: Element Ratios for Eight Solar Flares, Corrected for Mixing Effects: Model 2

	Element Ratios				
	Mg/Si	Al/Si	S/Si	Ca/Si	Fe/Si
MET 132826285-27185	0.76 ± 0.07	0.054 ± 0.031	0.053 ± 0.019	0.21 ± 0.03	2.92 ± 0.67
MET 134210436-12886	1.13 ± 0.10	0.085 ± 0.059	0.016 ± 0.026	0.02 ± 0.02	3.95 ± 1.60
MET 136508736-10886	0.79 ± 0.09	0.050 ± 0.065	0.006 ± 0.018	0.33 ± 0.14	5.13 ± 1.39
MET 136620036-21786	0.72 ± 0.09	0.019 ± 0.060	0.104 ± 0.081	0.11 ± 0.07	3.92 ± 1.08
MET 138677136-80836	1.00 ± 0.09	0.057 ± 0.055	0.020 ± 0.021	0.17 ± 0.06	1.98 ± 0.62
MET 153341842-42742	0.97 ± 0.09	0.003 ± 0.029	0.021 ± 0.009	0.07 ± 0.01	1.61 ± 0.37
MET 153418442-19292	1.07 ± 0.10	0.130 ± 0.038	0.013 ± 0.009	0.06 ± 0.02	4.18 ± 1.19
MET 153832142-34142	0.75 ± 0.07	0.098 ± 0.036	0.000 ± 0.006	0.13 ± 0.04	2.70 ± 0.67
Averages	0.869 ± 0.162	0.059 ± 0.041	0.011 ± 0.034	0.075 ± 0.099	2.373 ± 1.197



Table 4.21: Element Ratios for Eight Solar Flares, Corrected for  
Mixing Effects: Model 3

	Element Ratios			
	Mg/Si	Al/Si	S/Si	Ca/Si
MET 132826285-27185	0.74 ± 0.06	0.052 ± 0.031	0.066 ± 0.024	0.30 ± 0.05
MET 134210436-12886	1.13 ± 0.10	0.085 ± 0.059	0.016 ± 0.025	0.02 ± 0.02
MET 136508736-10886	0.79 ± 0.09	0.050 ± 0.066	0.006 ± 0.017	0.32 ± 0.14
MET 136620036-21786	0.73 ± 0.09	0.020 ± 0.060	0.099 ± 0.077	0.10 ± 0.06
MET 138677136-80836	1.00 ± 0.09	0.057 ± 0.055	0.019 ± 0.020	0.17 ± 0.06
MET 153341842-42742	0.97 ± 0.09	0.003 ± 0.029	0.020 ± 0.009	0.07 ± 0.01
MET 153418442-19292	1.07 ± 0.10	0.129 ± 0.038	0.014 ± 0.010	0.06 ± 0.02
MET 153832142-34142	0.78 ± 0.07	0.101 ± 0.036	-0.001 ± 0.006	0.12 ± 0.03
Averages	0.864 ± 0.159	0.059 ± 0.041	0.010 ± 0.034	0.073 ± 0.111
				2.437 ± 1.326

Table 4.22: Element Ratios for Eight Solar Flares, Corrected for Mixing Effects: Model 4

	Element Ratios			
	Mg/Si	Al/Si	S/Si	Ca/Si
MET 132826285-27185	0.66 ± 0.06	0.047 ± 0.029	0.069 ± 0.025	0.29 ± 0.05
MET 134210436-12886	1.11 ± 0.10	0.084 ± 0.059	0.017 ± 0.026	0.02 ± 0.02
MET 136508736-10886	0.74 ± 0.09	0.047 ± 0.064	0.006 ± 0.018	0.33 ± 0.14
MET 136620036-21786	0.66 ± 0.08	0.017 ± 0.057	0.104 ± 0.081	0.10 ± 0.06
MET 138677136-80836	1.00 ± 0.09	0.057 ± 0.056	0.018 ± 0.019	0.15 ± 0.05
MET 153341842-42742	0.97 ± 0.09	0.003 ± 0.029	0.019 ± 0.009	0.06 ± 0.01
MET 153418442-19292	1.07 ± 0.10	0.130 ± 0.038	0.013 ± 0.009	0.06 ± 0.02
MET 153832142-34142	0.69 ± 0.07	0.095 ± 0.035	-0.001 ± 0.006	0.12 ± 0.03
Averages	0.811 ± 0.193	0.057 ± 0.042	0.010 ± 0.036	0.067 ± 0.112
				2.108 ± 1.231

Table 4.23: Element Ratios for Eight Solar Flares, Corrected for  
Mixing Effects: Model 5

	Element Ratios				
	Mg/Si	Al/Si	S/Si	Ca/Si	Fe/Si
MET 132826285-27185	0.79 ± 0.07	0.061 ± 0.033	0.052 ± 0.020	0.23 ± 0.04	2.99 ± 0.69
MET 134210436-12886	1.09 ± 0.10	0.086 ± 0.060	0.015 ± 0.023	0.01 ± 0.02	3.14 ± 1.26
MET 136508736-10886	0.84 ± 0.10	0.055 ± 0.069	0.006 ± 0.015	0.30 ± 0.12	4.36 ± 1.18
MET 136620036-21786	0.78 ± 0.10	0.024 ± 0.065	0.092 ± 0.074	0.10 ± 0.06	3.22 ± 0.89
MET 138677136-80836	0.99 ± 0.09	0.058 ± 0.056	0.019 ± 0.019	0.15 ± 0.05	1.63 ± 0.51
MET 153341842-42742	0.97 ± 0.09	0.003 ± 0.028	0.019 ± 0.008	0.05 ± 0.01	1.18 ± 0.27
MET 153418442-19292	1.08 ± 0.10	0.131 ± 0.038	0.012 ± 0.009	0.05 ± 0.02	3.37 ± 0.95
MET 153832142-34142	0.79 ± 0.08	0.106 ± 0.037	0.000 ± 0.005	0.12 ± 0.03	2.33 ± 0.58
Averages	0.899 ± 0.132	0.062 ± 0.042	0.009 ± 0.031	0.059 ± 0.098	1.843 ± 1.021

Table 4.24: Element Ratios for Eight Solar Flares, Corrected for Mixing Effects: Model 6

	Element Ratios			
	Mg/Si	Al/Si	S/Si	Fe/Si
MET 132826285-27185	$0.79 \pm 0.07$	$0.056 \pm 0.033$	$0.074 \pm 0.028$	$8.15 \pm 1.89$
MET 134210436-12886	$1.05 \pm 0.10$	$0.083 \pm 0.059$	$0.015 \pm 0.023$	$3.47 \pm 1.40$
MET 136508736-10886	$0.84 \pm 0.10$	$0.054 \pm 0.069$	$0.006 \pm 0.016$	$5.32 \pm 1.44$
MET 136620036-21786	$0.78 \pm 0.10$	$0.023 \pm 0.065$	$0.094 \pm 0.075$	$3.84 \pm 1.06$
MET 138677136-80836	$0.99 \pm 0.09$	$0.058 \pm 0.056$	$0.018 \pm 0.019$	$1.63 \pm 0.51$
MET 153341842-42742	$0.98 \pm 0.09$	$0.003 \pm 0.029$	$0.019 \pm 0.008$	$1.31 \pm 0.30$
MET 153418442-19292	$1.06 \pm 0.10$	$0.128 \pm 0.038$	$0.014 \pm 0.010$	$5.83 \pm 1.69$
MET 153832142-34142	$0.80 \pm 0.08$	$0.106 \pm 0.037$	$0.000 \pm 0.005$	$2.82 \pm 0.70$
Averages	$0.896 \pm 0.121$	$0.061 \pm 0.041$	$0.009 \pm 0.034$	$1.981 \pm 2.294$

Table 4.25: Element Ratios for Eight Solar Flares, Corrected for Mixing Effects: Model 7

	Element Ratios				
	Mg/Si	Al/Si	S/Si	Ca/Si	Fe/Si
MET 132826285-27185	0.59 ± 0.05	0.044 ± 0.028	0.072 ± 0.026	0.30 ± 0.05	4.03 ± 0.93
MET 134210436-12886	1.09 ± 0.10	0.086 ± 0.060	0.015 ± 0.023	0.01 ± 0.02	3.16 ± 1.26
MET 136508736-10886	0.84 ± 0.10	0.055 ± 0.069	0.006 ± 0.015	0.31 ± 0.13	4.52 ± 1.22
MET 136620036-21786	0.78 ± 0.10	0.024 ± 0.065	0.093 ± 0.074	0.10 ± 0.06	3.31 ± 0.91
MET 138677136-80836	0.99 ± 0.09	0.058 ± 0.056	0.018 ± 0.019	0.15 ± 0.05	1.58 ± 0.49
MET 153341842-42742	0.97 ± 0.09	0.003 ± 0.028	0.019 ± 0.008	0.05 ± 0.01	1.18 ± 0.27
MET 153418442-19292	1.08 ± 0.10	0.130 ± 0.038	0.013 ± 0.009	0.05 ± 0.02	3.80 ± 1.08
MET 153832142-34142	0.79 ± 0.08	0.106 ± 0.037	0.000 ± 0.005	0.12 ± 0.03	2.40 ± 0.60
Averages	0.815 ± 0.172	0.057 ± 0.042	0.009 ± 0.034	0.059 ± 0.113	1.842 ± 1.185

Table 4.26: Average Elemental Ratios Derived from Eight Solar Flares (Including Mineral-Mixing Corrections)

Solar Model	Mg/Si	Al/Si	S/Si	Ca/Si	Fe/Si
Model 1	$0.861 \pm 0.162$	$0.059 \pm 0.041$	$0.011 \pm 0.036$	$0.079 \pm 0.111$	$2.374 \pm 1.308$
Model 2	$0.869 \pm 0.162$	$0.059 \pm 0.041$	$0.011 \pm 0.034$	$0.075 \pm 0.099$	$2.373 \pm 1.197$
Model 3	$0.864 \pm 0.159$	$0.059 \pm 0.041$	$0.010 \pm 0.034$	$0.073 \pm 0.111$	$2.437 \pm 1.326$
Model 4	$0.811 \pm 0.193$	$0.057 \pm 0.042$	$0.010 \pm 0.036$	$0.067 \pm 0.112$	$2.108 \pm 1.231$
Model 5	$0.899 \pm 0.132$	$0.062 \pm 0.042$	$0.009 \pm 0.031$	$0.059 \pm 0.098$	$1.843 \pm 1.021$
Model 6	$0.896 \pm 0.121$	$0.061 \pm 0.041$	$0.009 \pm 0.034$	$0.063 \pm 0.150$	$1.981 \pm 2.294$
Model 7	$0.815 \pm 0.172$	$0.057 \pm 0.042$	$0.009 \pm 0.034$	$0.059 \pm 0.113$	$1.842 \pm 1.185$

## 4.6 Future Work

It remains unclear whether the super-chondritic Fe/Si ratio is an artifact of the phase angle or whether it may be an actual surface phenomenon caused by space weathering or other regolith processes. In order to address this, we need to investigate phase-angle and other geometric effects on the Fe/Si and Ca/Si ratios through modelling and experimentation. Okada (2004) found that at particle sizes coarser than a certain limit ( $D > 45 \mu\text{m}$ ) the Ca/Fe and Ti/Fe ratios can become dependent on phase angle, declining by as much as 20% at  $\phi > 70^\circ$ .

The efforts of the “CHIANTI” team to improve their theoretical solar models continue. As new versions are released, they may be used to solve for the graded filter response function. Perhaps with an improved set of theoretical spectra, the filter model with the best  $\chi^2$  will coincide with the one that best matches the GOES data.

In an effort to investigate the cause of the observed sulfur depletion, Larry Nittler and others (including the present author) have undertaken (Nittler et al., 2003) to extract the Mn/Cr ratio from the XRS flare data. This ratio should not be strongly dependent on solar models because there are no solar emission lines between the K-edges of Mn and Cr. Fluorescence in both elements, therefore, should be excited almost exclusively by the solar Fe lines at 6.7–8 keV. Chromium is carried mainly in chromite, which is believed to melt at or near the Fe,Ni–FeS cotectic at about 950°C, whereas manganese is found mainly in mafic silicates

which do not begin to form a partial melt until about 1050°C. For this reason, primitive achondritic meteorites, which have experienced low degrees of partial melting, exhibit a variety of non-chondritic Mn/Cr ratios. Since chromium, unlike sulfur, is unlikely to be volatilized by micrometeorite impacts, the surface of a chondritic asteroid would probably retain its chondritic Mn/Cr ratio under space weathering.

#### **4.6.1 Future XRF Experiments**

The NEAR solar monitor had a number of serious shortcomings which should be avoided by future investigators. To be fair to the many dedicated people who worked on the XRF experiment, it should be said that they were hampered both by an abbreviated development schedule and by official restrictions on communication between the science and engineering teams while the instrument was designed and built.

The problems with the graded-filter design will have been suggested by the descriptions of the filter in Chapter 3 and of its postlaunch calibration in Chapter 4. The large number of free parameters (two pinhole diameters, thicknesses and densities of Kapton, Delrin, beryllium and aluminum layers) in the filter design ensured that post-launch calibration would be a complicated problem. The single worst design feature in this regard was the large ratio of the Delrin-layer thickness to the Delrin pinhole diameter (Figure 3.5) which made the solar monitor's response function strongly and unnecessarily sensitive to the incidence angle of



the Sun on the detector. Even had the solar monitor been calibrated on the ground, a large number of measurements at various source-detector geometries would have been needed in order to adequately characterize its angular response.

The possibility of non-concentric positions of the Be and Delrin pinholes has not been addressed in the preceding chapters, but of course opens up a whole additional range of azimuthally dependent “solutions” to the solar monitor response function. It is unlikely that the existing data are adequate to solve for such an azimuthal dependence.

In sensitivity, the gas solar monitor fell between two stools. With the graded filter, it was not sensitive enough to enable easy interpretation of the solar spectra measured during non-flaring, “quiet Sun” periods. During flares, however, the detector suffered from baseline shift (§3.5.2) due to the inability of the electronics to handle the high count rates properly; and by the end of the mission the detector aging caused by repeated exposure to high count rates was expressed in gain changes and degraded resolution. Future solar monitor designs should take into account the very great dynamic range required to monitor the Sun in X-rays.

It would be desirable, although perhaps technically challenging, to be able to measure solar flux directly in the energy regions that actually induce the light-element fluorescence: the Mg XII lines at  $\sim 8.4 \text{ \AA}$  (1.5 keV), the Si XIII line at  $6.6 \text{ \AA}$  (1.9 keV), the Si XIV lines at  $6.2 \text{ \AA}$  (2 keV), and the S XV and XVI lines at  $4.7\text{--}5.0 \text{ \AA}$  ( $\sim 2.5\text{--}2.6$  keV). This would allow

the solar data to be interpreted without the heavy reliance on theoretical solar models (such as those of Mewe et al. (1985) and the “CHIANTI” group) that has characterized the NEAR analysis.

In order to obtain accurate Fe/Si compositions, it would be crucial for these low-energy solar measurements to be absolutely calibrated with respect to a measurement of flux from the 6-8 keV solar Fe structures.

## BIBLIOGRAPHY

- Acton, L. W., Finch, M. L., Gilbreth, C. W., Culhane, J. L., Bentley, R. D., Bowles, J. A., Guttridge, P., Gabriel, A. H., Firth, J. G., Hayes, R. W. 1980. The soft X-ray polychromator for the Solar Maximum Mission. *Solar Physics* 65, 53-71.
- Berger, M. J. and J. H. Hubbell, *XCOM: Photon Cross Sections on a Personal Computer*, NBSIR 87-3597 (1987), National Institute for Standards and Technology, U.S.A. Data extracted from the XRAY data base of the IAEA Nuclear Data Information System.
- Bergstrom, P. M., Pratt, R. H. 1997. An overview of the theories used in Compton scattering calculations. *Radiation Physics and Chemistry* 50, 3-29.
- Boynton, W. V., and 22 colleagues 2001. Elemental Composition of Asteroid 433 Eros: Results from the NEAR-Shoemaker X-Ray/Gamma-Ray Spectrometer and Comparison with Meteorites. *Meteoritics & Planetary Science*, vol. 36, Supplement, p.A27 36, 27.
- Chantler, C.T., Olsen, K., Dragoset, R.A., Kishore, A.R., Kotochigova, S.A., and Zucker, D.S. (2003), *X-Ray Form Factor, Attenuation and Scattering Tables (version 2.0)*. [Online] Available: <http://physics.nist.gov/ffast> [Access date].
- National Institute of Standards and Technology, Gaithersburg, MD. Originally published as Chantler, C.T., *J. Phys. Chem. Ref. Data* 29(4),

- 597-1048 (2000); and Chantler, C.T., J. Phys. Chem. Ref. Data 24, 71-643 (1995).
- Clark, P. E., Trombka, J. I. 1997. Remote X-ray spectrometry for NEAR and future missions: Modeling and analyzing X-ray production from source to surface. *Journal of Geophysical Research* 102, 16361-16384.
- Compton, A. H. 1923. The Spectrum of Scattered X-Rays. *Physical Review* 22, 409-413.
- Compton, A. H. 1923. A Quantum Theory of the Scattering of X-rays by Light Elements. *Physical Review* 21, 483-502.
- Cullity, B. D. and S. R. Stock 2001. *Elements of X-Ray Diffraction, Third Edition*. Prentice-Hall, Upper Saddle River, NJ.
- Dere, K. P., Landi, E., Mason, H. E., Monsignori Fossi, B. C., Young, P. R. 1997. CHIANTI - an atomic database for emission lines. *Astronomy and Astrophysics Supplement Series* 125, 149-173.
- Dere, K. P., Landi, E., Young, P. R., Del Zanna, G. 2001. CHIANTI-An Atomic Database for Emission Lines. IV. Extension to X-Ray Wavelengths. *Astrophysical Journal Supplement Series* 134, 331-354.
- Doschek, G. A., Fludra, A., Bentley, R. D., Lang, J., Phillips, K. J. H., Watanabe, T. 1990. On the dependence of solar flare X-ray spectral line intensity ratios of highly ionized sulfur, calcium, and iron on electron temperature, differential emission measure, and atomic physics. *Astrophysical Journal* 358, 665-673.

- Evans, L. G., Starr, R. D., Brückner, J., Reedy, R. C., Boynton, W. V., Trombka, J. I., Goldstein, J. O., Masarik, J., Nittler, L. R., McCoy, T. J. 2001. Elemental composition from gamma-ray spectroscopy of the NEAR-Shoemaker landing site on 433 Eros. *Meteoritics and Planetary Science* 36, 1639-1660.
- Feldman, U. 1992. Elemental abundances in the upper solar atmosphere. *Physica Scripta* 46, 202.
- Feldman, U., Mandelbaum, P., Seely, J. F., Doschek, G. A., Gursky, H. 1992. The potential for plasma diagnostics from stellar extreme-ultraviolet observations. *Astrophysical Journal Supplement Series* 81, 387-408.
- Feldman, U., Doschek, G. A., Behring, W. E., Phillips, K. J. H. 1996. Electron Temperature, Emission Measure, and X-Ray Flux in A2 to X2 X-Ray Class Solar Flares. *Astrophysical Journal* 460, 1034.
- Feldman, U., Doschek, G. A., Mariska, J. T., Brown, C. M. 1995. Relationships between Temperature and Emission Measure in Solar Flares Determined from Highly Ionized Iron Spectra and from Broadband X-Ray Detectors. *Astrophysical Journal* 450, 441.
- Feldman, U., Widing, K. G. 1990. Photospheric abundances of oxygen, neon, and argon derived from the XUV spectrum of an impulsive flare. *Astrophysical Journal* 363, 292-298.

- Fludra, A., Schmelz, J. T. 1995. Absolute Abundances of Flaring Coronal Plasma Derived from SMM Spectral Observations. *Astrophysical Journal* 447, 936.
- Fludra, A., Doyle, J. G., Metcalf, T., Lemen, J. R., Phillips, K. J. H., Culhane, J. L., Kosugi, T. 1995. Evolution of two small solar flares.. *Astronomy and Astrophysics* 303, 914.
- Freeland, S. L., and Handy, B. N., 1998. "Data Analysis with the Solar-Soft System." *Solar Physics* 182, 497.
- Garcia, H. A. 1994. "Temperature and emission measure from GOES soft X-ray measurements." *Solar Physics* 154, 275-308.
- Goldsten, J. O., and 15 colleagues 1997. "The X-ray/Gamma-ray Spectrometer on the Near Earth Asteroid Rendezvous Mission." *Space Science Reviews* 82, 169-216.
- Hapke, B. 2001, *J. Geophys. Res.*, 10039
- Hubbell, J., 1969. *Photon cross-sections, attenuation coefficients, and energy absorption coefficients from 10 keV to 100 GeV*. Rep. NSRDS-NBS 29, Nat. Bur. Stand., Washington D.C., USA. 80 pp.
- Hubbell, J. H. 1997. "Summary of existing information on the incoherent scattering of photons, particularly on the validity of the use of the incoherent scattering function." *Radiation Physics and Chemistry* 50, 113-124.

- Hubbell, J. H., Seltzer, S. M., 1997. *Tables of x-ray mass attenuation coefficients and mass energy- absorption coefficients*. National Institute of Standards and Technology, Gaithersburg, Maryland, USA.
- Hubbell, J. H., Veigele, W. J., Briggs, E. A., Brown, R. T., Cromer, D. T., Howerton, R. J. 1975. Atomic form factors, incoherent scattering functions, and photon scattering cross sections. *J. Phys. Chem. Ref. Data* 4, 471-538.
- Kaastra, J.S., Mewe, R., 1993. *Legacy* 3, 16.
- Knoll, G. F., 2000. *Radiation Detection and Measurement, Third Edition*. New York, John Wiley & Sons.
- Lachance, G. R. and Claisse, F. 1995. *Quantitative X-ray Fluorescence Analysis: Theory and Application*. New York, John Wiley & Sons.
- Lin, R. P., and 65 colleagues 2002. The Reuven Ramaty High-Energy Solar Spectroscopic Imager (RHESSI). *Solar Physics* 210, 3-32.
- McCoy, T. J., and 16 colleagues 2001. The composition of 433 Eros: A mineralogical-chemical synthesis. *Meteoritics and Planetary Science* 36, 1661-1672.
- McTiernan, J. M., Fisher, G. H., Li, P. 1999. The Solar Flare Soft X-Ray Differential Emission Measure and the Neupert Effect at Different Temperatures. *Astrophysical Journal* 514, 472-483.
- Mewe, R., Gronenschild, E. H. B. M., van den Oord, G. H. J. 1985. Calculated X-radiation from optically thin plasmas. V. *Astronomy and Astrophysics Supplement Series* 62, 197-254.

- Mewe, R., Kaastra, J.S., Liedahl, D.A., 1995. *Legacy* 6, 16.
- Meyer, J.-P. 1985. Solar-stellar outer atmospheres and energetic particles, and galactic cosmic rays. *Astrophysical Journal Supplement Series* 57, 173-204.
- Nittler, L. R., Clark, P. E., McCoy, T. J., Murphy, M. E., & Trombka, J. I. 2000. Bulk Compositional Trends in Meteorites: A Guide for Analysis and Interpretation of NEAR XGRS Data from Asteroid 433 Eros. *Lunar and Planetary Institute Conference Abstracts*, 31, 1711
- Nittler, L. R., and 14 colleagues 2001. X-ray fluorescence measurements of the surface elemental composition of asteroid 433 Eros. *Meteoritics and Planetary Science* 36, 1673-1695.
- Nittler, L. R., Lim, L., McCoy, T. J., Starr, R. D., Burbine, T. and McClanahan, T. 2003. A Search for the Minor Elements Mn, Cr and Ni in NEAR-Shoemaker X-ray Spectra from 433 Eros.
- Okada, T. 2004, *Lunar and Planetary Institute Conference Abstracts*, 35, 1927
- Peres, G., Orlando, S., Reale, F., Rosner, R., Hudson, H. 2000. The Sun as an X-Ray Star. II. Using the Yohkoh/Soft X-Ray Telescope-derived Solar Emission Measure versus Temperature to Interpret Stellar X-Ray Observations. *Astrophysical Journal* 528, 537-551.
- Phillips, K. J. H., Mewe, R., Harra-Murnion, L. K., Kaastra, J. S., Beiersdorfer, P., Brown, G. V., Liedahl, D. A. 1999. Benchmarking



- the MEKAL spectral code with solar X-ray spectra. *Astronomy and Astrophysics Supplement Series* 138, 381-393.
- Phillips, K. J. H. 2004. The Solar Flare 3.8-10 keV X-Ray Spectrum. *Astrophysical Journal* 605, 921-930.
- Pierazzo, E., Vickery, A. M., Melosh, H. J. 1997. A Reevaluation of Impact Melt Production. *Icarus* 127, 408-423.
- Pieters, C. M., et al. 2000, *Meteoritics & Planetary Science*, vol. 35, Supplement, p.A127, 35, 127
- Pieters, C. M., Englert, P. A. J. 1993. Remote Geochemical Analysis, Elemental and Mineralogical Composition. Remote Geochemical Analysis, Elemental and Mineralogical Composition, ISBN 0521402816, Cambridge University Press, 1993. .
- Sasaki, S., Nakamura, K., Hamabe, Y., Kurahashi, E., & Hiroi, T. 2001, *Nature*, 410, 555
- Schwartz, R. A., 1998. Version 6 of GOES\_TRANSFER.PRO. In the Solarsoft package (Freeland and Handy 1998).
- Seely, J. F., Feldman, U., Doschek, G. A. 1987. Observation of nonthermal energy distributions during the impulsive phase of solar flares. *Astrophysical Journal* 319, 541-554.
- Starr, R., and 16 colleagues 2000. Instrument Calibrations and Data Analysis Procedures for the NEAR X-Ray Spectrometer. *Icarus* 147, 498-519.

- Sterling, A. C., Doschek, G. A., Feldman, U. 1993. On the absolute abundance of calcium in solar flares. *Astrophysical Journal* 404, 394-402.
- Sylwester, J., Lemen, J. R., Mewe, R. 1984. Variation in observed coronal calcium abundance of X-ray flare plasmas. *Nature* 310, 665.
- Sylwester, J., Lemen, J. R., Bentley, R. D., Fludra, A., Zolcinski, M.-C. 1998. Detailed Evidence for Flare-to-Flare Variations of the Coronal Calcium Abundance. *Astrophysical Journal* 501, 397.
- Thomas, R. J., 2003. GOES\_TF.PRO, in the Solarsoft package (Freeland and Handy 1998), available at <http://www.lmsal.com/solarsoft/>.
- Thomas, R. J., Crannell, C. J., Starr, R. 1985. Expressions to determine temperatures and emission measures for solar X-ray events from GOES measurements. *Solar Physics* 95, 323-329.
- Trombka, J. I., and 12 colleagues 1997. Compositional mapping with the NEAR X ray/gamma ray spectrometer. *Journal of Geophysical Research* 102, 23729-23750.
- Trombka, J. I., and 21 colleagues 2001. The NEAR-Shoemaker x-ray/gamma-ray spectrometer experiment: Overview and lessons learned. *Meteoritics and Planetary Science* 36, 1605-1616.
- Trombka, J. I., and 23 colleagues 2000. The Elemental Composition of Asteroid 433 Eros: Results of the NEAR-Shoemaker X-ray Spectrometer. *Science* 289, 2101-2105.

- Yoshimori, M., Okudaira, K., Hirasima, Y., Igarashi, T., Akasaka, M., Takai, Y., Morimoto, K., Watanabe, T., Ohki, K., Nishimura, J. 1991. The wide band spectrometer on the Solar-A. *Solar Physics* 136, 69-88.
- Young, P. R., Del Zanna, G., Landi, E., Dere, K. P., Mason, H. E., Landini, M. 2003. CHIANTI-An Atomic Database for Emission Lines. VI. Proton Rates and Other Improvements. *Astrophysical Journal Supplement Series* 144, 135-152.